Excitation and Dispersion of a Rossby Wave Train on the Polar Jet by an Extra-tropical Transition of a Hurricane

Roni Ravia

Department of Atmospheric and Oceanic Sciences
McGill University, Montreal

August 2006

A thesis submitted to the Faculty of Graduate Studies and Research in partial fulfilment of the requirements of the degree of Masters of Science.

Your file Votre référence
ISBN: 978-0-494-32776-0
Our file Notre référence
ISBN: 978-0-494-32776-0

Acknowledgments

I would like to thank all those people who constantly gave me their support throughout my research project. First of all, I wish to express my sincere gratitude to my supervisors Dr. Gilbert Brunet and Prof. Peter Yau, who guided this work and helped whenever I was in need. Their feedback and their patience were invaluable.

I am also indebted to Prof. David Dritschel from St. Andrews University for kindly letting us use his CASL numerical model and for the technical support. His endless patience and detailed e-mails were truly priceless.

I am grateful for my faculty comrades; especially to Alexandra Jahn, Ruben Santos, Xingbao Wang, Badri Nagarajan, Irena Paunova and Amal El Akkraoui. Special thanks to the departmental system administrator, Marc Lanctot for his exceptional assistance.

I acknowledge the financial support by the Foundation for Climate and Atmospheric Science (CFCAS) which made this research possible.

Finally, I would like to express my deepest gratitude for the constant support, understanding and love that I have received from my partner Alex and from my parents during the past years.

Abstract

The enhanced potential vorticity gradients along the polar jet serve as a wave guide for trapped Rossby waves. These tropopause level, synoptic scale Rossby waves are of primary importance for weather development at the surface. In particular, extreme weather events have been linked to the existence of overlying upper level meridionally elongated filaments of stratospheric (high potential vorticity) air which form during the breaking of these waves. Motivated by the desire to understand the conditions under which these waves are formed and to improve their predictability, the current thesis discusses one excitation mechanism – the potential vorticity anomaly associated with a hurricane approaching the extra-tropics.

Attention is directed toward the adiabatic interaction of the cyclone with the polar jet before the two features meet. The hurricane's ability to excite Rossby waves is verified from observations of past interactions and theoretical study using a mechanistic model with idealized settings. The nature of the interaction between the cyclone and the polar jet is found to be sensitive to parameters such as the cyclone's radius and PV anomaly. Three different regimes have been identified. It is also concluded that the same parameters have influence on the skill of the Rossby wave prediction. The more intense the cyclone is, the harder it is to accurately predict the response of the polar jet.

Résumé

Les forts gradients du tourbillon potentiel le long du jet polaire servent de train d'onde pour les ondes de Rossby piégées. Ces ondes de Rossby d'échelle synoptique existant au niveau de la tropopause, sont d'une importance majeure pour le développement des perturbations en surface. En particulier, des événements extrêmes ont été associés à l'existence, dans les niveaux supérieurs, d'une superposition de filaments méridionaux d'air stratosphérique (fort tourbillon potentiel). Motivée par le désir de comprendre les conditions de formation de ces ondes et d'améliorer leur prévisibilité, cette thèse traite d'un mechanisme d'excitation – l'anomalie du tourbillon potentiel associée à un cyclone se rapprochant des zones extra-tropicales.

Une attention particulière est portée sur l'interaction adiabatique du cyclone avec le jet polaire avant que les deux structures se rencontrent. La capacité d'un cyclone à exciter des ondes de Rossby est vérifiée par des observations d'interactions et une étude théorique dans un cadre idéalisé. Il a été trouvé que la nature des interactions entre le cyclone et le jet polaire est sensible à des paramètres tels que le rayon du cyclone et l'anomalie du tourbillon potentiel. Trois différents régimes ont été identifiés. Il a aussi été conclue que ces mêmes paramètres influencent la précision de la prédiction de l'onde de Rossby. Plus le cyclone est intense, plus il est difficile d'adéquatement prédire la réaction du jet polaire.

Contents

Chapter 1

Introduction

1.1 Motivation

THORPEX is an international research program which strives to improve short term high-impact weather forecasts (*Shapiro and Thorpe*, 2004). The THORPEX International Science Plan (*Shapiro and Thorpe*, 2004) outlines numerous core objectives. One of them is to "Increase knowledge of global-to-regional influence on the initiation, evolution and predictability of high-impact weather". To achieve this objective, the excitation of a Rossby wave train by an extra-tropical cyclone development is mentioned as a future research goal due to the fact that "the skillfull prediction of Rossby wave-train activity is often a requisite for forecasting the synoptic-scale setting within which smaller-scale, high-impact weather events evolve at forecast time ranges out to two weeks".

In the course of this thesis we chose to center our attention on excitation of a Rossby wave train on the polar jet. These tropopause level westerly flow disturbances (i.e. synoptic scale Rossby waves) are of primary importance for the weather development at the surface (*Hoskins et al.*, 1985; *Petterssen and Smebye*, 1971) and have been reported to trigger extreme weather events (*Martius*, 2005). Therefore, it is highly important to gain knowledge on how these waves are excited. Among several triggers for excitation of these synoptic scale Rossby waves, we chose to focus on extra-tropical transition of a hurricane (from now on ETH). We strive to show that the interaction of the ETH with the polar jet will initiate a Rossby wave train development. We believe that understanding the nature of the interaction and determining the resolution needed for representing it with sufficient accuracy in a numerical model, will contribute to the improvement of medium-range forecast skill.

1.2 Rossby waves restoring mechanism

1.2.1 Qualitative description

In a general discussion of Rossby waves, *Hoskins et al.* (1985) attributed the existence of Rossby waves to potential vorticity (PV) gradients on isentropic surfaces. Using conservation of Rossby-Ertel PV [1] on isentropic surfaces, they considered the real basic state in which the isentropic potential vorticity (IPV) gradient is directed northward. A sinusoidal disturbance (adiabatic and frictionless) forced upon the basic state will acquire a pattern of positive (for southward displacement) and negative (for northward displacement) IPV anomalies. The perturbed PV field will induce a meridional wind field which in turn, causes parcels that have not been displaced to move southward (northward) by the negative IPV anomaly to their west (east) and the positive IPV anomaly to their east (west) (*Guinn and Schubert*, 1993). This PV advection process will result in a westward propagating wave – the Rossby wave. The process which has just been described has been termed in the literature as the "Rossby wave restoring mechanism".

Vortex Rossby waves: It is conventional to associate Rossby waves with planetary Rossby waves whose existence depends on the global PV gradients (i.e. the change of Coriolis parameter with latitude). However, the restoring mechanism concept holds for the locally enhanced PV gradients along the polar jet as well (*Martius*, 2005). Perhaps the most distinctive feature of the polar jet stream is its accompanying PV distribution which "takes the form of a band of enhanced potential vorticity gradient" (*Schwierz et al.*, 2004). Although the latitudinal variation of Coriolis parameter contributes to the existence of this band, gradients of relative vorticity due to the curvature and shear of the wind along the jet play a much bigger role. Rossby waves

[1] $Rossby - ErtelPV = -g\,(\zeta_\theta + f)\,\frac{\partial\theta}{\partial p}$

which exist on jets were discussed in the literature in the context of hurricane spiral bands (*MacDonald*, 1968; *Guinn and Schubert*, 1993; *Montgomery and Kallenbach*, 1997; *Chen et al.*, 2003) and were first termed "vortex Rossby waves" by *Montgomery and Kallenbach* (1997). However, since we focus on Rossby waves which exist on the polar jet, it is somewhat misleading to call these Rossby waves "vortex Rossby waves". Nevertheless, the separation between the "mid-latitude tropopause level Rossby waves" and the "planetary Rossby waves" remains essential. Throughout this thesis, we refer to these Rossby waves by the name "synoptic scale Rossby waves" or simply "Rossby waves" in order to maintain the conventional terminology, but we keep in mind that these are nothing but "vortex Rossby waves".

1.2.2 Quantitative description

A deeper insight on the role of jets in the Rossby wave restoring mechanism can be gained by the derivation of the dispersion relation for barotropic Rossby waves. We begin by considering the shallow water non-divergent PV equation

$$\frac{d}{dt}(\zeta + f) = 0 \tag{1.1}$$

where $\frac{d}{dt} = \frac{\partial}{\partial t} + u\frac{\partial}{\partial x} + v\frac{\partial}{\partial y}$ and $u = -\frac{\partial}{\partial y}\psi$, $v = +\frac{\partial}{\partial x}\psi$, $\zeta = \frac{\partial}{\partial x}v - \frac{\partial}{\partial y}u = \nabla^2\psi$ are the non-divergent wind field and vorticity (written in terms of the streamfunction) respectively. We now decompose the velocity field into a basic state and perturbation components. A flow setting such as the one exhibited by a jet can be represented by a basic state where the zonal wind component changes with latitude and where the meridional wind components is zero. The perturbed wind field and vorticity $u = u_0(y) + u' = u_0(y) - \frac{\partial}{\partial y}\psi'$, $v = v' = +\frac{\partial}{\partial x}\psi'$, $\zeta = -\frac{d}{dy}u_0 + \nabla^2\psi'$ are introduced into equation (1.1). The resultant linearized equation is given by

$$\left(\frac{\partial}{\partial t} + u_0\frac{\partial}{\partial x}\right)\nabla^2\psi' + \left(\frac{df}{dy} - \frac{d^2u_0}{dy^2}\right)\frac{\partial\psi'}{\partial x} = 0 \tag{1.2}$$

Assuming a plane wave solution $\psi' = Ae^{i(kx+ly-\omega t)}$ leads to the following dispersion relation

$$\omega = u_0 k - \frac{k\left(\frac{df}{dy} - \frac{d^2u_0}{dy^2}\right)}{k^2+l^2} \tag{1.3}$$

The first term on the right hand side of equation (1.3) represents a Doppler shift due to the basic state wind. The second term is the meridional gradient of absolute vorticity for which the global vorticity gradient and the local vorticity gradient along the polar jet are the two contributors. The zonal phase velocity is given by equation (1.4).

$$c = \frac{\omega}{k} = u_0 - \frac{\frac{df}{dy} - \frac{d^2u_0}{dy^2}}{k^2+l^2} \tag{1.4}$$

As discussed qualitatively in Subsection 1.2.1, equation (1.4) clearly shows that the phase velocity is always westward relative to the basic zonal flow. A Rossby wave can become stationary (i.e. independent of time) when

$$K_s^2 = k^2 + l^2 = \frac{\frac{df}{dy} - \frac{d^2u_0}{dy^2}}{u_0} \tag{1.5}$$

Rossby wave-guides: Wave guides are preferred pathways on which waves propagate (*Martius*, 2005). Rossby wave guides are characterized by regions of maximum K_s (*Hoskins and Ambrizzi*, 1993 as discussed in *Martius*, 2005). When discussing Rossby waves on the polar jet, the local vorticity gradient (second term on the right hand side of equation 1.5) is the main contributor in fulfilling the condition of maximum K_s (see Subsection 1.2.1). Therefore, the polar jet is known to serve as a wave guide for trapped Rossby waves (*Schwierz et al.*, 2004).

1.3 Rossby wavebreaking and high-impact weather events

"The term wavebreaking for Rossby waves simply refers to a rapid, irreversible deformation of material contours" (*Holton*, 1992). The existence of a "critical layer" (*Haynes*, 1989 and references therein) has been reported to play a major role in the dynamics of wavebreaking. These layers are regions where the phase speed of the wave approaches the mean flow speed. When that happens, nonlinear effects can no longer be neglected and wavebreaking occurs. Synoptic Rossby waves in the upper tropopause appear to break predominantly outward, ejecting high PV values towards the equator (*Hoskins et al.*, 1985 as discussed in *Nakamura and Plumb*, 1994). *Nakamura and Plumb* (1994) attribute the one sided wavebreaking to the effects of "flow asymmetry" – that is, the asymmetry in the location of the critical layers. They explain that the velocity distribution around the polar jet is usually such that the critical layer south of the jet is located closer to the jet than the one to the north. Thus, a wave of certain amplitude, propagating on the jet, might reach the critical layer to the south of the jet but not the one north of it, resulting in wavebreaking only towards the equator. They further note that whether or not the wave would break depends on its amplitude. If the wave's amplitude is too small, there will be no wavebreaking at all and viscous effects will dominate. If it is large enough, wavebreaking is feasible on both sides of the jet.

Appenzeller and Davies (1992) have coined the term "potential vorticity streamer" when referring to the meridionally elongated filaments of stratospheric (high PV) air which form during the breaking of synoptic scale Rossby waves. *Martius* (2005) mentions numerous upper and lower level processes of which PV streamers have influence on. One of these processes is the formation of heavy precipitation along the south side of the Alps. The strong dependence of high-impact weather (i.e. heavy precipitation) events over Europe on the existence of an overlying upper level PV streamers is well established in the work of *Martius* (2005). As PV streamers form during the breaking of synoptic scale Rossby waves, a Rossby wave train is a precursor to heavy precipitation events (*Grazzini and van der Grijn*, 2002; *Blackburn et al.*, 2003; *Krishnamurti et al.*, 2003; *Shapiro*, 2004; *Shapiro and Thorpe*, 2004; *Martius*, 2005). It is for this reason that we decided to investigate one potential triggering mechanism for excitation of Rossby wave train on the polar jet.

1.4 Extratropical transition of a hurricane as a triggering mechanism

Jones et al. (2003) mention two mechanisms by which a tropical cyclone can modify the extra-tropical circulation: "the adiabatic interaction between the PV of a tropical cyclone and that of a midlatitude jet, and the impact of diabatically modified PV on the midlatitude circulation". When referring to the evolution of the polar jet, the latter refers to the intense tropopause level ridge generated by the cyclone's transport of warm and moist air (low PV) into the extra-tropic (*Martius*, 2005) and the concomitant appearance of an enhanced trough downstream (east to the cyclone) due to the southward advection of high PV air by the tropical cyclone's upper level, diabatically generated anticyclone (*Habjan and Holland*, 1995 as discussed in *Ferreira and Schubert*, 1999). The former mechanism refers to the excitation of short Rossby wave by the PV anomaly associated with the tropical cyclone and the dispersion of its energy (*Ferreira and Schubert*, 1999; *Schwierz et al.*, 2004). In the present work, we will focus solely on the former.

By using an adiabatic, inviscid, shallow water model (see Chapter 3), inter-level interaction and diabatic effects are eschewed. Similar "dry dynamics" simulations have been performed by *Ferreira and Schubert* (1999). Using an adiabatic, frictionless, shallow water model they investigate the interaction between a tropical cyclone and upper tropospheric PV gradients over the tropics (which is derived from the circumpolar vortex). They acknowledge the fundamental roles that diabatic effects and vertical stratification play in the evolution of the PV gradients and hence justify their study by noting that: "This barotropic study is but a first step toward understanding the complicated nonlinear patterns of interaction between the circumpolar vortex and a tropical cyclone. Further work on the interaction of tropical cyclones with the circumpolar vortex using a multilayer global model that includes diabatic effects is obviously needed". In the same sense, we stress that our current work is by no means a complete comprehensive research on the ETH-polar jet interaction but an attempt to shed light on certain aspects of the problem.

In addition, we would like to remark on an issue that needs to be clarified. The present work has been named "excitation and dispersion of a Rossby wave train on the polar jet by an extra-tropical transition of a hurricane". The specific choice of ETH and not hurricane is intentional and justified by the assumption that the influence of a tropical cyclone on the polar jet through "action at a distance" (see explanation in the next paragraph) is significant only when the tropical cyclone is relatively close to the jet and as such, is likely to have lost most of its tropical characteristics. It is hard to define exactly when a tropical cyclone underwent an extra-tropical transition but a variety of factors (such as loss of warm core, loss of wind field symmetry, increase in radius of gale force winds etc.) are usually taken into consideration by different operational centers (*Jones et al.*, 2003). Thus, the title of the thesis does not imply that adiabatic interaction with the polar jet is impossible when the cyclone is still regarded as a hurricane. As a matter of fact, in all three case studies presented in Chapter 2 the majority of the interaction stages occurs when the cyclone is still considered (by NOAA National Hurricane Center) to be a hurricane. Thus, our title is meant to convey simply the sense of the proximity of the cyclone to the jet and perhaps also to shift the focus away from hurricane related diabatic effects and direct it to the adiabatic aspects of the interaction.

The adiabatic interaction between the ETH and the polar jet is based on the theoretical concept of "action at a distance" (*Bishop and Thorpe*, 1994 as discussed in *Jones et al.*, 2003). In their article, *Bishop and Thorpe* (1994) give theoretical basis for the concept of "action at a distance" which they define as the "cornerstone of PV thinking". They draw the analogy between electrical charges and PV anomalies and state that in the same way that electrical charges induce an electrical field, "quasi-geostrophic PV charges" induce a field, and it is this field that implies action at a distance. In that sense this idea "seeks to attribute to a feature on the weather chart, such as a vorticity anomaly, a unique influence on the rest of the atmosphere" (*Bishop and Thorpe*, 1994). In relation to our work, the term "action at a distance" refers to the concept by which the circulation associated with positive PV (i.e. the ETH), can excite a Rossby wave on the PV gradients associated with the polar jet, before the PV anomalies of the two features meet (*Jones et al.*, 2003). Clearly, such influence does not occur at infinite distance but is controlled by the Rossby radius of deformation.

Excitation of Rossby waves on PV gradients by a PV anomaly through "action at a distance" was previously discussed in the literature. *Ferreira and Schubert* (1999) discuss the role of tropical cyclones in the formation of tropical upper tropospheric troughs (TUTT) and their later evolution into a cut-off cyclone that wanders into the tropics (TUTT cells). Their study bears great resemblance to ours in the sense that they present the formation of a Rossby wave train on the tropopause level PV gradients over the tropics due to the adiabatic interaction with a tropical cyclone. Moreover, they are using a shallow water model and the tropical cyclone is represented by a circular patch of cyclonic vorticity. They indicate that the simulation of the interaction between an upper tropospheric feature such as the tropopause level PV gradients and that of a primarily lower tropospheric feature such as a tropical cyclone (which is a warm core system with cyclonic PV that maximizes at the surface and decreases with height) might be problematic in a shallow water model. However, they argue that one can regard a tropical cyclone as a "deep (surface to tropopause) positive anomaly of potential vorticity". In relation to what we have discussed earlier when we commented on the intentional choice of an ETH over a hurricane, we use this argument to stress that whether the numerical experiments (presented later on in Chapter 4) simulate a hurricane or an ETH is irrelevant in the sense that the representation of the cyclone as a positive PV anomaly remains valid for both features. The major differences between the studies is the fact that the PV gradients of the polar jet are sharper than the zonally averaged summer tropospheric PV gradients over the tropics that *Ferreira and Schubert* (1999) considered. Moreover, the cyclone is embedded in an anticyclonic flow in their study whereas in our study it is embedded in a strong cyclonic flow.

Schwierz et al. (2004) examined the interaction between a vortex forcing and the polar jet in an idealized setting where the jet is zonally aligned. Using a nonlinear numerical (hemispheric primitive equations) model, they performed experiments with various forcing configurations including: mesoscale vortex of positive PV, synoptic-scale vortex of positive/negative PV and a hybrid setup of both orographically bound negative anomaly and an advecting surface-based positive thermal anomaly. Their model has 27 vertical layers but as initial conditions, they placed the zonally aligned jet and the juxtaposed vortex-like anomaly only at tropopause level and examined the evolution of that level only.

In our study, experiments are performed with an adiabatic, inviscid, f plane, quasi-geostrophic, shallow water model based on contour dynamics (see Chapter 3) written by D. G. Dritschel. In the paper by *Schwierz et al.* (2004), the jet was a zonally aligned transition zone of strong horizontal PV gradient between two regions of uniform PV. In the model we are using, further simplification in the representation of the polar jet has been implanted. The polar jet is simply represented by circular patch of constant positive PV. The ETH is represented in the model in the same way – a patch of strong, positive PV at the level of the polar jet. In other words, the continuous PV gradients of a jet (the polar jet and the ETH jet) are replaced by a PV interface. Such interfaces are commonly known in the literature by the name "PV fronts" (*Bell*, 1990). The idealized configuration where horizontal PV gradient of a jet is completely concentrated in such a front has a long pedigree in atmospheric and oceanic sciences (*Schwierz et al.*, 2004). In particular, the motion of such fronts is often calculated numerically by means of contour dynamics (*Stern and Pratt*, 1985; *Pratt and Stern*, 1986; *Polvani and Plumb*, 1992; *Nakamura and Plumb*, 1994; *Ambaum and Verkley*, 1995; *Swanson et al.*, 1997; *Scott et al.*, 2004). The idea of considering such a simplified analog to the polar jet and the ETH is attractive for numerous reasons. First, mechanistic models provide the simplest way in which one can test various physical processes. Moreover, the use of such models enables one to achieve very high resolution at short simulation time and with modest computing resources (*Polvani and Plumb*, 1992). Using a mechanistic model of contour dynamics is particularly beneficial. As a Lagrangian method, contour dynamics tend to concentrate resolution in the vortex structure and hence might be better suited in the simulation of the mutual interaction between two vortices (*Dritschel*, 1989) as discussed in Chapter 3.

The uniqueness of ETH relative to other extra-tropical cyclones is twofold. First, it is perhaps a more intensified PV anomaly due to stronger characteristic winds and smaller radius as compare to the majority of extra-tropical cyclones. Second, it always approaches the jet from the south and thus is embedded in a lower PV environment (as opposed to the flow setting in the numerical simulations done by *Schwierz et al.* (2004) where the vortex PV anomaly was always embedded in the high PV environment to the north of the jet).

1.5 Aims and outline

The main objective of this thesis is first and foremost, to verify whether the interaction between the ETH and the polar jet can indeed lead to excitation of Rossby waves on the PV gradients of the jet. The verification will be conducted by examination of observations of past hurricane-jet interactions and investigation of the adiabatic interaction using a mechanistic (quasi-geostrophic, shallow water, f plane, adiabatic and frictionless) contour dynamic model. With the aid of the model, we would like to understand the nature of the interaction as a function of the ETH's radius and the strength of its PV anomaly (or in other words, its PV gradient). The last objective of this thesis is related to improving medium-range weather forecasting. *Jones et al.* (2003) warns that "If the interactions between a tropical cyclone and the mid-latitude PV gradients at upper level are misrepresented in a forecast model, there is likely to be an impact on developments downstream and thus a reduction in skill of medium range forecasts". Based on resolution numerical experiments, using the mechanistic model, and keeping in mind its limitations, we would like to have a rough estimation regarding the spatial resolution needed in order to represent the ETH-polar jet interaction with sufficient accuracy. In addition, we would like to see whether the skill of the Rossby wave prediction depends on the intensity of the ETH.

The thesis is organized as follows. In Chapter 2 three cases of hurricane-jet interaction are studied in order to verify similar behaviour of Rossby wave train excitation. Chapter 3 discusses the fundamentals of the model we are using for conducting numerical simulations as well as a brief review of contour dynamics and contour surgery. The advantages of the model for our purposes are also presented. Chapters 4 and 5 discuss the results of the numerical experiments focusing respectively on different flow settings and varying resolutions. The concluding discussion will appear in Chapter 6.

Chapter 2

Case studies

Through consideration of three case studies, the present Chapter demonstrates the excitation of a Rossby wave train on the polar jet by a hurricane approaching the extra-tropics. As discussed at the beginning of Section 1.4, there are two ways in which a tropical cyclone may trigger a Rossby wave train on the polar jet. Even though this thesis focuses on the adiabatic process alone, in the case studies presented here, both diabatic (at the stage where the cyclone still maintains tropical characteristics) and adiabatic processes (due to the strong positive PV anomaly) potentially assist in the excitation of the wave train. No attempt was made to quantify the influence of each mechanism separately as this is beyond the scope of this thesis. It is implicitly assumed that both mechanisms contribute to the excitation of the Rossby wave train to some extent. The "dry dynamics" experiments presented later in Chapter 4 are performed in order to isolate the effect of the adiabatic mechanism exclusively.

2.1 Case studies

In order to clearly demonstrate Rossby wave excitation by a hurricane, we have chosen to present cases with a flow setting where the strong polar jet located above the north Atlantic Ocean is relatively zonal and the hurricane approaching it from the south-west remains sufficiently strong during its transition into the extra-tropics. The synoptic history and best track data are based on NOAA National Hurricane Center's Atlantic tropical cyclones preliminary reports (*Lawrence*, 2000, *Lawrence*, 1996 and *Pasch*, 1999).

Figures 2.1, 2.3 and 2.5 show PV fields on the $350K$ isentrope for a period of three to four days for each of the three cases. The data used for these plots is the ECMWF ERA-40 data set with a high resolution of approximately $125km$ in the horizontal and 60 levels stretched over $65km$ in the vertical (*Martius*, 2005). In the $350K$ isentropic surface, the tropopause is co-located with the meandering belt of strong PV gradients in the midlatitudes (*Ferreira and Schubert*, 1999). Since the 2 PVU contour is conventionally taken as tropopause level, the jet stream is presented in these figures by the overlying 2 PVU surface isotachs. The location of the hurricane (or its later extra-tropical transition) is pointed out by a black filled circle added manually to the figures. The hurricane's positive PV anomaly does not appear strongly or does not appear at all due to inadequate data resolution. Also note that due to the hurricane's warm core, the PV anomaly at this elevation is not at its peak. Even though the excitation of the Rossby wave train on the polar jet by the approaching hurricane is evident in these figures, a more vivid depiction of the wave train is available through figures 2.2, 2.4 and 2.6. These figures present a Hövmoller diagram of the 2 PVU surface meridional wind at the 45°N latitude (note that the wind isotachs overlying the PV maps in figures 2.1, 2.3 and 2.5 refer to the wind speed whereas these figures refer to the meridional wind component). Characteristics of the wave train will be discussed with the aid of these figures.

2.1.1 Hurricane Gert case

Tropical storm Gert became a hurricane on September 13^{th} 1999 near 16°N, 39°W. It continued to strengthen to 130 knots by the 16^{th} and maintained high winds of around 115 knots through the 19^{th}. Gradual weakening of the cyclone commenced on the 20^{th}. Nevertheless, the cyclone maintained "hurricane force" winds and low pressure values up until 00 UTC September 23^{rd} when it was downgraded to a tropical storm.

At 00 UTC September 21^{st} (figure 2.1(a)), Hurricane Gert was located at 29°N, 63°W with wind speed of 95 knots and minimum pressure of 950 mb. At the same time, an almost zonally aligned polar jet (and its accompanying enhanced band of PV gradients) was located to its north-east at around the 45°N latitude. Twenty four hours later (figure 2.1(b)), as the hurricane progressed north-east and was now located at 34°N, 61°W, a Rossby wave pattern was starting to form with the ridge axis positioned right above the hurricane and the trough axis located 30° longitude to its east. Another twenty four hours have passed (figure 2.1(c)), and as the hurricane continued its progress into the mid-latitudes, the ridge and trough deepened and slightly moved eastward. By 12 UTC September 23^{rd}, (figure 2.1(d)) hurricane Gert was located at 47°N, 52°W. It was now downgraded to a tropical storm as its winds decreased to 60 knots and its surface pressure now stood at 964 mb. On the other hand, the trough to the east of the hurricane continued to deepen into lower latitudes (25°N). In addition, it is increasingly becoming more elongated and with a north-east south-west orientation.

An additional insight on the wave train's characteristics is available through examination of figure 2.2. A wave-two pattern is clearly demonstrated through this figure. The wave train is excited on September 21^{st} with the first appearance of a trough, represented by a sequence of blue (negative meridional wind component) and red (positive meridional wind component) patches, upstream of the hurricane's location. Since the Hövmoller diagram focuses on the 45°N latitude, the ridge (red-blue sequence) located right above the hurricane and the downstream trough, 30° longitude to its east, become more distinct only a day later on the 22^{nd}. The deepening of the trough approaching the European Atlantic coast is demonstrated by the high values (negative and positive) of the meridional wind component which peak on September 24^{th}. The above mentioned trough clearly represents the largest amplitude

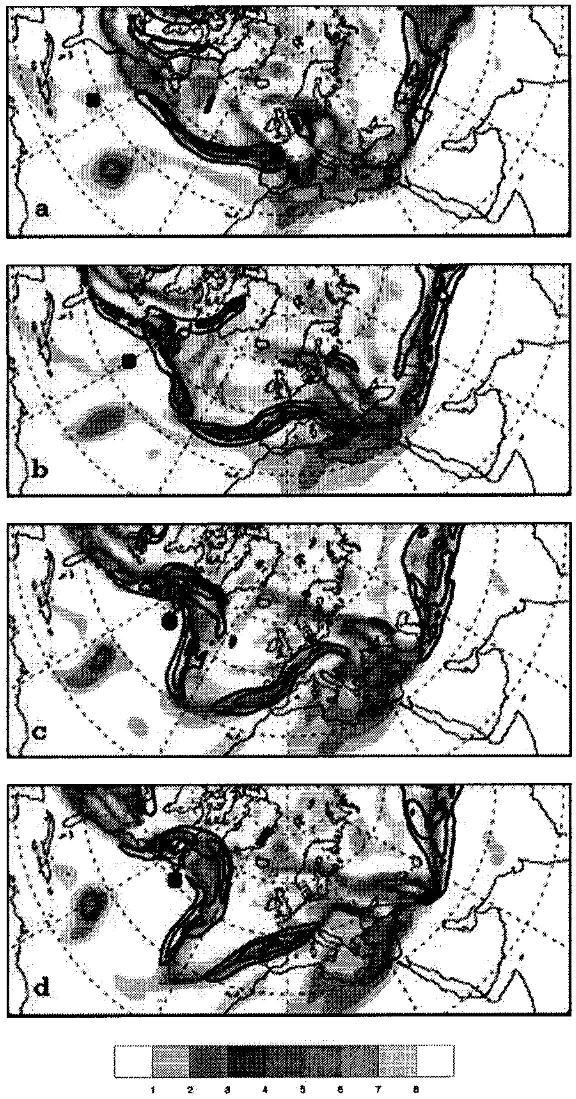

Figure 2.1: Evolution of PV (shaded, PV units) on a 350K isentrope and isotachs (thick black lines, 40,50,60 m/sec) on a 2 PVU surface overlaid at a) 00 UTC 21 Sep 1999, b) 00 UTC 22 Sep, c) 00 UTC 23 Sep and d) 12 UTC 23 Sep. Position of hurricane Gert is marked with a black circle

of this Rossby wave train. The wave train's propagation speed can be calculated by the slope of a line crossing the maximum-minimum center (not shown). Calculations reveal value of approximately $2000 km/day$ ($26°/day$). The wave train lasted for approximately eight days.

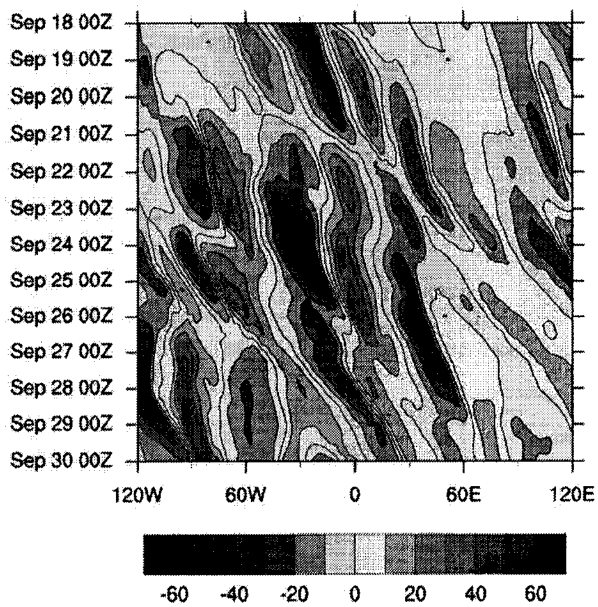

Figure 2.2: Hövmoller diagram of the meridional wind (m/sec) at 45°N on the 2 PVU surface during September 1999.

2.1.2 Hurricane Jose case

Tropical storm Jose became a hurricane late on the 19^{th} of October 1999 near 15°N, 59°W and reached its peak intensity with 85 knots wind, eighteen hours later. The hurricane then gradually started to weaken due to the south-westerly vertical shear (*Pasch*, 1999) only to be downgraded to a tropical storm at mid-day October 21^{st}.

At 00 UTC October 23^{rd} (figure 2.3(a)), tropical storm Jose was located at 22°N, 65°W with wind speed of 50 knots and minimum pressure of 994 mb. At the same time, an almost zonally aligned polar jet (and its accompanying enhanced band of PV gradients) was located to its north-east at around the 45°N latitude. Twenty four hours later (figure 2.3(b)), as the hurricane progressed north-eastward and was located at 27°N, 63°W, a Rossby wave pattern was starting to form. This time (unlike in hurricane Gert's case), the wave's position was shifted eastward by about 10^o longitude (i.e., the ridge axis was positioned around 10° longitude east of Jose and the subsequent trough at 40°). At mid-day October 24^{th}, satellite intensity estimates indicated that Jose regained hurricane strength (*Pasch*, 1999). The resurrection of the hurricane didn't last long though. At 00 UTC on the 25^{th} (figure 2.3(c)), hurricane Jose was once again downgraded to a tropical storm and as it kept its steady progress into higher latitudes, the ridge and trough deepened and slightly moved eastward. At 12 UTC October 25^{th} Jose was declared (according to NOAA National Hurricane Center) extra-tropical and by 18 UTC (figure 2.3(d)), it was absorbed by a larger extra-tropical cyclone. At that time, the trough continued to deepen and penetrated into lower latitudes (25°N). In addition, it is increasingly becoming more elongated and tilted slightly in a north-east south-west orientation.

The wave train pattern is once again demonstrated by the use of a Hövmoller diagram in figure 2.4. A wave-two pattern is clearly demonstrated in this figure. The wave train is excited on October 21^{st} with the first appearance of a trough (blue-red sequence) upstream of the location of the hurricane, which occured later at 00 UTC October 22^{nd}. The ridge (red-blue) and trough (blue-red) east of Jose are clearly visible in the diagram on the 24^{th}. The

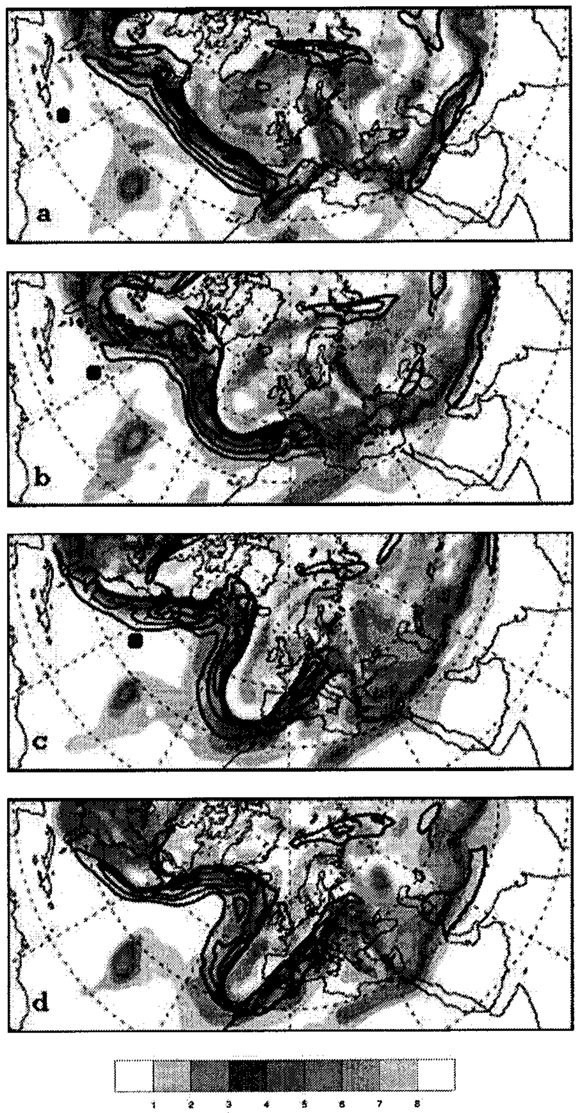

Figure 2.3: Evolution of PV (shaded, PV units) on a 350K isentrope and isotachs (thick black lines, 40,50,60,70 m/sec) on a 2 PVU surface overlaid at a) 00 UTC 23 Oct 1999, b) 00 UTC 24 Oct, c) 00 UTC 25 Oct and d) 18 UTC 25 Oct. Position of hurricane Jose is marked with a black circle.

deepening of the trough approaching the European Atlantic coast translates into high values (negative and positive) of the meridional wind component which peak on October 25^{th}. This trough represents the largest amplitude of this Rossby wave train. The wave train lasted for about six days and the estimated propagation speed is around $3000km/day$ ($40°/day$). Note the existence of an earlier, slightly weaker Rossby wave train (see upper half portion in figure 2.4). This wave train was excited by hurricane Irene which traveled through the North Atlantic Ocean prior to hurricane Jose.

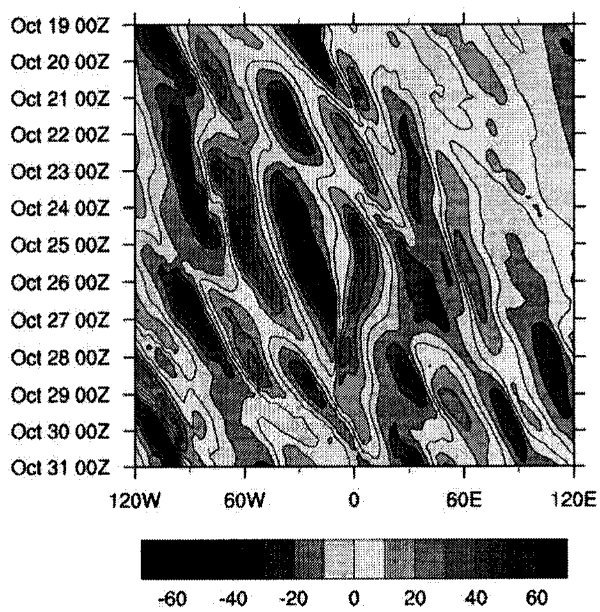

Figure 2.4: Hövmoller diagram of the meridional wind (m/sec) at 45°N on the 2 PVU surface during October 1999.

2.1.3 Hurricane Luis case

Tropical storm Luis became a hurricane late on August 30^{th} 1995 near 14°N, 37°W. It continued to strengthen to 120 knots by the 3^{rd} of September and maintained high winds of around 115-120 knots for the next four days. Gradual weakening of the cyclone commenced on September 7^{th}. Nevertheless, the cyclone maintained "hurricane force" winds and low pressure values up until 12 UTC September 11^{th} when it was declared (according to NOAA National Hurricane Center) extra-tropical and its wind speed dropped below 65 knots.

At 00 UTC September 10^{th} (figure 2.5(a)), Hurricane Luis was located at 34°N, 67°W with wind speed of 85 knots and a minimum pressure of 959 mb. At the same time, an almost zonally aligned polar jet (and its accompanying enhanced band of PV gradients) was located to its north-east at around the 45°N latitude. Twelve hours later (figure 2.5(b)), as the hurricane progressed north-east and was now located at 38°N, 64°W, a Rossby wave pattern was starting to form. As in hurricane Jose's case, the ridge's axis was positioned around 10° longitude east of hurricane Luis. Since the jet stream had a small extent in the first place (it was not stretched over the entire length of the Atlantic ocean as it was in the two previous cases we have discussed), the trough is now defined from a PV perspective only (intrusion of dry stratospheric air into lower latitudes) rather than a distinct wave pattern on the jet itself. Nevertheless, the jet does seem to bend south-eastward and is positioned on the western bank of the PV trough. Another twelve hours have passed (figure 2.5(c)), and as the hurricane continued its progress into the midlatitudes, the ridge and trough pattern deepened and the trough's axis began to tilt towards the south-west. At 12 UTC September 11^{th} (figure 2.5(d)), hurricane Luis was located at 46°N, 52°W and was declared extra-tropical. The trough to the east was now thin, north-east south-west oriented and its tip reached the 20°N latitude. Due to the small

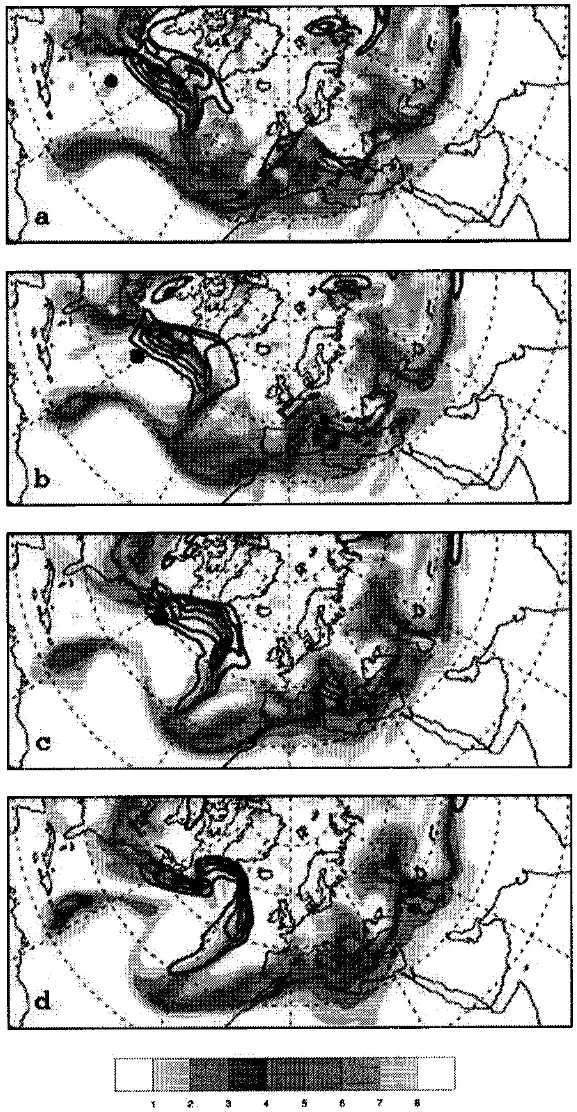

Figure 2.5: Evolution of PV (shaded, PV units) on a 350K isentrope and isotachs (thick black lines, 40,50,60,70 m/sec) on a 2 PVU surface overlaid at a) 00 UTC 10 Sep 1995, b) 12 UTC 10 Sep, c) 00 UTC 11 Sep and d) 12 UTC 11 Sep. Position of hurricane Luis is marked with a black circle.

extent of the jet stream (discussed in the previous paragraph), it is difficult to discern the signature of the Rossby wave train in the Hövmoller diagram of the 2 PVU meridional wind component (figure 2.6). The initial (around 70°W) and final (around 60°E) minimums are very weak. Nevertheless, the diagram is able to capture the main feature of the interaction – the elongated deep PV trough approaching the European coast around September 12^{th}. The peak anomaly is a reflection of the north-south tilting of the jet and is located in the region of the west side of the PV trough depicted in figure 2.5(d).

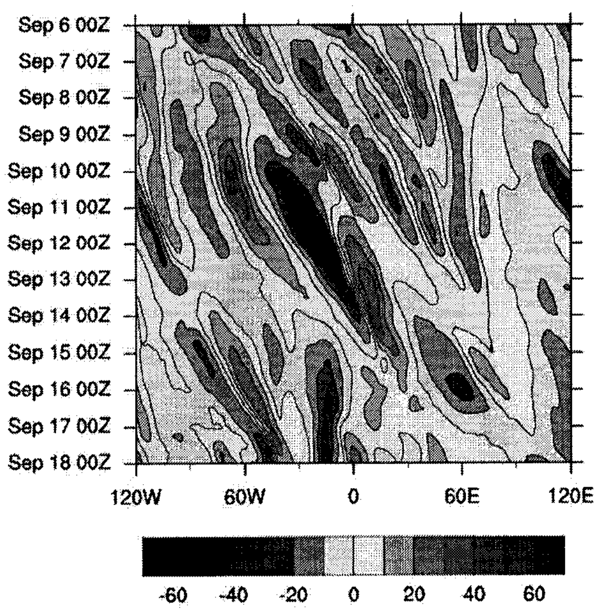

Figure 2.6: Hövmoller diagram of the meridional wind (m/sec) at 45°N on the 2 PVU surface during September 1995.

2.2 Discussion

In an attempt to summarize the interaction between the hurricane and the polar vortex as seen in the three cases presented in the previous section, a few points come to mind. Dispersion of Rossby wave energy and the formation of a wave train are exhibited in all three cases. For all cases, the wave train is initiated at the time where the hurricane is situated away from the jet. This validates the "action at a distance" hypothesis which has been discussed in Section 1.4. In addition, a similar sequence of events is evident – an initial zonally aligned polar jet that eventually develops a deep trough which digs deep into the tropics. Even though other disturbances exist in the atmosphere which might as well trigger Rossby wave excitation, the presence of a hurricane at the same time of the wave excitation surely can not be taken as mere coincidence.

An interesting point to note is that, apart from a very short period in the case of hurricane Jose, where a slight increase in the wind speed occurred, Rossby wave amplitude increase was always accompanied by a decrease in the hurricane's intensity. This connection suggests an exchange of energy between the hurricane and the polar vortex.

A close look at figures 2.1 and 2.3 reveals the existense of a cell of upper tropospheric (high PV) air wandering into the tropics. Figure 2.5 sheds light on its origin. As discussed by *Ferreira and Schubert* (1999), a thinning mid-latitude upper tropospheric trough may eventually roll up into a large cyclone that will become cut off from the polar vortex. *Ferreira and Schubert* (1999) refer to them as TUTT (tropical upper tropospheric troughs) cell. Such upper level cyclones are also mentioned by *Schwierz et al.* (2004). The reason for the existence of the elongated, thin upper tropospheric troughs from which the cell in the above mentioned figures was originated can be Rossby wave excitation by an earlier hurricane or it could be baroclinic wave development in which an upper tropospheric trough penetrates the lower latitudes and becomes elongated in the anticyclonic shear of this environment (*Thorncroft et al.*, 1993 as discussed in *Ferreira and Schubert*, 1999). This upper level cyclone does not possess sharp PV gradients such as those existed in a hurricane. As such, its influence on the polar vortex through "action at a distance" is negligible.

Chapter 3

The model

All numerical experiments included in the current thesis are performed using the Contour-Advective Semi-Lagrangian (CASL) model written by D. G. Dritschel and described in the article: "The CASL algorithm for quasi-geostrophic flow in a cylinder" (*Macaskill et al.*, 2003) and references therein.

3.1 Contour dynamics review

3.1.1 Two dimensional flows and vortices

In practice, one can consider flows in the atmosphere and ocean to be approximately two dimensional due to the constraints of both the Earth's rotation and its density stratification. Stratification suppresses vertical motion and rotation weakens the dependence of the fluid motions on the coordinate along the rotational axis (*Vosbeek*, 1998; *Macaskill et al.*, 2003). The dynamics of quasi two-dimensional vortices is a major component in the study of the large-scale atmospheric and oceanic two-dimensional flows, so called geophysical flows (*Vosbeek*, 1998). On constant θ surfaces, PV is conserved in the absence of diabatic and viscous effects and thus it is natural to define vortices by regions of constant PV (*Macaskill et al.*, 2003). These "piecewise uniform" PV patches evolve when embedded in a PV gradient (such as the one produced by another PV patch, for example) and the scientific study of their evolution has a long history. *Dritschel* (1989) claims that since Eulerian methods are unable to tailor resolution into areas of strong vorticity, their suitability for simulations of the dynamics of vortices is questionable. On the other hand, he notes that Lagrangian methods, which follow individual fluid particles as they move about in space, conserving their PV, are capable to concentrate resolution in the vortex's structure and as such can produce greater accuracy in the simulation of two dimensional vortices. *Dritschel and Ambaum* (1997) summarize by saying that conservative, advected fields, handled in a Lagrangian representation of contours on two dimensional surfaces, are retained to scales well below computational grid scale and thus, this type of representation is much less dissipative. Contour dynamics is one Lagrangian method which is widely used in the field of two-dimensional vortex dynamics.

3.1.2 Contour dynamics

The method of contour dynamics was originally invented by Zabusky, Hughes and Roberts (*Zabusky et al.*, 1979) and has greatly evolved over the years mainly through the work of Dritschel (*Dritschel*, 1989 and references therein).

"The term "contour dynamics" means the dynamics of boundaries of vorticity discontinuity (contours); implicit is the assumption that the vorticity distribution is piecewise constant" (*Dritschel*, 1989). Contour dynamics uses the fact that, in a two dimensional, inviscid and incompressible flows, the same fluid particles remain on the boundaries at all times and hence, evolution of a patch of uniform vorticity is fully determined by the instantaneous position of its bounding contour (*Dritschel*, 1989; *Vosbeek*, 1998). The assumption of piecewise constant vorticity does not prevent contour dynamics from obtaining a realistic approximation to the real life vortices as domains of different vorticity are achieved by introducing several contours (*Dritschel*, 1989).

In general, this is how the method works. The PV field is represented by contours of PV discontinuity. These contours are represented by finite number of nodes. The number of nodes is adjustable. If during the calculations they move apart significantly, extra nodes are added in order to maintain high accuracy. The number of nodes can also be reduced if required. The velocity is recovered from the PV field at each time step by contour integration. In turn, the recovered flow field advects the nodes to their new position. Contour integrals are performed once again on the newly located contour and the process repeats (*Macaskill et al.*, 2003). The most powerfull tool of contour dynamics has always been its ability to maintain high resolution in regions where the greatest changes take place (by the insertion of additional nodes), but this has also been its greatest source of weakness (*Macaskill et al.*, 2003). *Macaskill et al.* (2003) explain: "the filamentation of vorticity, and the corresponding generation of smaller and smaller scales, may give rise to an exponential growth in the number of nodes, all in the pursuit of PV features that are almost certainly not dynamically significant". The overwhelming number of nodes which need to be added in order to cope with this rapid development of small scale features was computationally unmanageable (*Dritschel*, 1989).

3.1.3 Contour surgery

Motivated by the need to deal with the formation of "regions of fast-growing curvature", Dritschel introduced, in the late 80's, a fundamental extension to contour dynamics – a technique called "contour surgery".(*Dritschel*, 1988). This extension to contour dynamics has proved to be a crucial step in the evolution of contour dynamics as it has greatly improved its numerical efficiency. The technique overcomes the build-up of small scale structures by removing contour features that are smaller than a prescribed length scale. In other words, contour dynamics stops resolving accurately parts of the contour whose radius of curvature becomes comparable with this predetermined length scale (*Dritschel*, 1989). Contour surgery either truncates or joins contours, depending on the condition (*Macaskill et al.*, 2003). If a contour has been broken, contour surgery will also topologically reconnects the remaining parts of that contour, resulting in two new contours (*Macaskill et al.*, 2003).

An important comment has to be made. In an inviscid fluid, contours cannot break or join together and thus surgery errors are viewed as a numerical approximation just like the approximations of finite temporal and spatial resolution (*Dritschel*, 1989). This is an important note to keep in mind when we later observe the simulation of ETH-polar jet performed with the model. Although in reality, the jet does exhibit a behaviour of severe deformation and at times breaking of PV filaments in the form of cut-off low (see discussion in Section 1.3), the newly formed contours that are ejected from the main PV contour of the jet in the experiments presented in Chapters 4 and 5 are merely a numerical error due to contour surgery and are not physically meaningful.

Contour surgery's reasoning for neglecting small scales features is based on the assumption that they have "little dynamical importance" and "negligible effect on the large scale dynamics" (*Dritschel*, 1988). Variety of tests has been performed in order to evaluate the accuracy of the technique. It was found that errors produced by surgery are comparable to the errors produced in the contour dynamics part of the algorithm (due to approximations of finite temporal and spatial resolution) and thus, just like with any other approximation, its validity cannot be stretched for arbitrarily long times (*Dritschel*, 1988).

3.2 Model description

3.2.1 The governing equations

The model employs the quasi-geostrophic approximation where the dynamical evolution of the flow is governed by the conservation of PV according to the quasi-geostrophic PV (from now on QGPV) equation. By choosing to work with one layer (as we did), the model will effectively revert to the shallow water QGPV equation:

$$\left(\frac{\partial}{\partial t} - \left(\frac{1}{r}\frac{\partial \psi}{\partial \theta}\right)\frac{\partial}{\partial r} + \frac{\partial \psi}{\partial r}\left(\frac{1}{r}\frac{\partial}{\partial \theta}\right)\right) q = 0 \tag{3.1}$$

where

$$q = f + \nabla^2 \psi - \frac{f^2}{gD}\psi + \frac{f}{D}h_B \tag{3.2}$$

We make further simplification by choosing to work with flat bottom (i.e. no topography) so that the last term on the right hand side of equation (3.2) is neglected to yield

$$q = f + \nabla^2 \psi - \frac{f^2}{gD}\psi \tag{3.3}$$

The first term on the right hand side of equation (3.3) is the Coriolis parameter, the second term is the relative vorticity while the third term is the contribution to the QGPV due to changes of the free surface height.

3.2.2 The CASL numerical method

Even though surgery was able to limit the complexity of contour dynamics by removing filaments smaller than a prescribed scale and topologically reconnect parts of the same contour that are closer than the same prescribed scale, the computation of contour integrals continued to be an expensive process (*Macaskill et al.*, 2003; *Dritschel and Ambaum*, 1997). Nevertheless, the advantages of contour dynamics for accurate dynamical description of conservative, advected fields is priceless. Driven by the desire to benefit from the accuracy of contour dynamics, but at the same time to be able to eliminate the expensive aspects of it (i.e. computation of contour integrals), *Dritschel and Ambaum* (1997) came up with a novel numerical algorithm called "contour-advective semi-Lagrangian (CASL)". Relying on the concept of "contour advection" (*Waugh and Plumb*, 1994; *Norton*, 1994), the CASL is a hybrid Lagrangian-Eulerian numerical algorithm for simulating the evolution of fine-scale conservative fields in two dimensional QG flows (*Macaskill et al.*, 2003; *Dritschel and Ambaum*, 1997). This algorithm is able to enjoy the advantages of two approaches. High resolution is maintained by the use of contour surgery and the expensive computation of contour integrals for the recovery of the advecting velocity is replaced by the interpolation of the PV field on a grid and the use of Eulerian techniques to compute its associated velocity field.

In general, the CASL algorithm operates according to the following steps (more detailed description of the algorithm is given in *Dritschel and Ambaum* (1997)):

- PV field is initially represented by contours with a specific jump in PV (Lagrangian)
- PV field is converted from the contour representation onto a grid (Lagrangian $\longrightarrow$ Eulerian)
- the velocity field is recovered from the grided PV field on a coarser grid by the use of equation (3.3)
- the velocity is interpolated back onto the irregular location of the contour nodes (Eulerian $\longrightarrow$ Lagrangian)

- the advection of the nodes is executed using the Runge-Kutta scheme, according to equation (3.1) (Lagrangian)
- surgery is performed and the nodes are redistributed
- return to the first step for calculations of the next time step

"The inherent assumption of the CASL algorithm is that the velocity field is required at significantly lower resolution than the PV field, but that the PV may still be accurately tracked in time. Calculations up to the present time have supported this assumption which is made plausible by the fact that the spectral width of the velocity is much narrower than that of a PV" (*Macaskill et al.*, 2003). As a matter of fact, the PV field is retained on a grid 2^x times finer than the one which is used for the recovery of the velocity field. In that way, the most costly step in the CASL algorithm (the recovery of the velocity field by PV inversion) is done on a coarse grid (*Dritschel and Ambaum*, 1997). It is possible to specify the fine/coarse grid ratio (i.e. to specify x) in the CASL model. We will use $x = 2$ as used by *Scott et al.* (2004).

The spatial resolution of the model is determined by the resolution of contour surgery (which is related to the number of nodes). Surgery in the CASL model operates at resolution, approximately 10 times finer than that of the velocity grid (*Dritschel and Ambaum*, 1997). The resolution of the velocity grid can be specified by the user (see Subsection 3.2.3). The time stepping in the CASL model is relatively large, approximately on the advective time scale (*Dritschel and Ambaum*, 1997). The use of a large time step is made possible by the fact that there is no time step restriction for numerical stability (*Macaskill et al.*, 2003). Nevertheless, the ability to maintain solution accuracy while using a large time step is yet another advantage of the model. For spatial and temporal resolution specifications for the numerical experiments, the readers are referred to Subsection 3.2.3.

3.2.3 Model settings

By choosing one of the available options in the model, the initial flow setting becomes two circular vortices of uniform PV. One of the vortices is fixed to the center of the domain and the other is free to move with the ambient flow. In our case, the fixed vortex represents the polar jet and the advected vortex represents the ETH. For each vortex, the user specifies the PV jump (interior - exterior) and the radius. An f plane is assumed and a cylindrical shallow water layer is chosen as our domain. Spatial and temporal resolutions are user defined. The spatial resolution for the coarse grid on which the advecting velocity is recovered, is determined through specification of the number of waves. The number of azimuthal intervals $\Delta\theta$ is twice the number of waves and the number of radial intervals Δr is half the number of azimuthal intervals. We chose to execute the "radially variable grid spacing" option where $\Delta r = \Delta s^2$ so that the spacing in r is more dense as one approaches the origin. This uneven distribution of radial intervals is a recommended option for problems such as the study of polar vortex where one wishes to focus on the dynamics near the origin and away from the influence of the boundaries (*Macaskill et al.*, 2003). The number of nodes is determined by the model as a function of the user specified velocity grid resolution. As noted in Subsection 3.2.2, the number of nodes is adjusted by surgery throughout the experiment but in general, the resolution of the contour representation is about 10 times finer than the resolution of the velocity grid. In addition, the initial distance between the vortex centers should be determined by the user along with the Rossby radius of deformation and the temporal resolution. All the above mentioned user defined parameters which were chosen for our numerical experiments are specified in Chapters 4 and 5.

One additional issue with regard to the model setting needs to be addressed. The model in fact works in two stages. In the second stage, the evolution of the two vortices is followed. The process by which the evolution is calculated in the model has been described in Subsection 3.2.2. However, a preliminary stage is executed prior to this. During that stage, the two vortices are pushed towards each other with a small strain rate (small enough to keep the vortices in near equilibrium as they are pushed together) while the model is slowly generating a family of near equilibrium states. As explained by *Dritschel* (1995), between inelastic interaction, vortices evolve through a sequence of near-equilibrium states. Once this equilibrium proves to be unstable, rapid, unstable motion proceeds. This motion is the inelastic interaction itself and this is where the code of the CASL switches into stage two. Due to the operation of these two stages, we would like to introduce the following terminology: *initial state* refers to the initial conditions, the state where the two vortices are in the shape of two perfectly circular contours, whereas, *t=0* refers to the stage where equilibrium breaks and the evolution of the interaction ensues. The time it takes to reach *t=0* from the initial state is not physically meaningful and is considered as "model initialization time".

Chapter 4

Numerical experiments 1 - various flow settings

The nature of the adiabatic interaction between the ETH and the polar jet is tested in this Chapter through consideration of different flow setting (i.e. different ETH radii and PV anomalies).

4.1 Specified parameters

In our experiments using the CASL model, the domain is a cylindrical layer (shallow water) with radius $r = 1$. This non-dimensional radius represents a value of $12000km$. The Rossby radius of deformation in that layer is taken to be $1000km$ to match the conventional value associated with upper tropospheric dynamics (*Nakamura and Plumb*, 1994). The non-dimensional Rossby radius of deformation is thus 1/12. The radius of the circular patch of vorticity which represents the polar jet is fixed to be $4500km$ with a non-dimensional value of 0.375. The radius of the patch representing the ETH changes with each experiment spanning $300km$, $500km$ and $700km$ (corresponding to 0.025, 0.0416 and 0.0583 respectively). The PV outside the contours is set to be the Coriolis parameter (i.e., the relative vorticity is set to zero) in order to ensure decay of the polar jet and the ETH jet at larger radii (*Nakamura and Plumb*, 1994). The PV jump across the interface of the fixed circle (in our simulation, the polar jet) is fixed in the model and is given the non-dimensional value of 1. The PV across the interface of the advected circle (in our simulation, the ETH) is chosen with respect to this value. In other words, the user specifies the ETH/polar jet PV ratio. In our numerical experiments, the PV ratio changes with each experiment with values of 1, 2.5 and 4. The reasoning behind choosing these values is as follows. By applying dimensional analysis to equation (3.3), the dimensional PV inside the contour of each vortex can be approximated by $PV_{vortex} = fR_0$ where R_0 is the Rossby number of the considered vortex. Thus, for the polar jet, we considered a Rossby number of 0.5 (arrived at by assuming a wind gradient of $100m/sec$ across a distance of $2000km$ with a Coriolis parameter of $10^{-4}sec^{-1}$) similar to the value taken by *Nakamura and Plumb* (1994) for the polar jet in their experiments. For the ETH, values of the Rossby number varies between 2 (for ETH with radius of $300km$, this value corresponds to characteristic tropopause level winds of $60m/sec$), for unusually intense ETH, and 0.5 for a weak ETH. These approximations result in a PV ratio between 1 (for identical Rossby number of 0.5 for the two features) to 4 (when Rossby number of the ETH is taken to be 2).

The time is non-dimensionalized with respect to the PV jump across the polar jet interface. One time unit in the model is equivalent to $2\pi/PV_{jet}$ seconds. Recalling that $PV_{vortex} = fR_{0_{vortex}}$, one model time unit corresponds to $2\pi/fR_{0_{jet}} = \pi/\Omega R_{0_{jet}} = 0.5/R_{0_{jet}} days$. By choosing 0.5 as the approximated value of the Rossby number of the polar jet, we specified one model time unit as one day.

The spatial resolution is specified for the grid on which the advecting velocity is recovered by specifying the number of waves. The approximated resolution of the model is 10 times finer than the resolution for recovering the advective velocity (see explanation in Subsections 3.2.3). For all experiments in this Chapter, we have chosen to work with 128 waves, resulting in a model resolution of 2560 even azimuthal intervals and 1280 uneven radial intervals. At the vicinity of the jet, these values correspond to ($\frac{2\pi\cdot 4500}{2560} \simeq$) $11km$ and ($\Delta r_{\frac{4500\cdot 1280}{12000}} \simeq \Delta s^2_{480} = 12000 \cdot ((\frac{480}{1280})^2 - (\frac{479}{1280})^2) \simeq$) $7km$ for azimuthal and radial intervals respectively (see Subsection 3.2.3 for clarification).

The temporal resolution in all experiments is five percent of the advective time scale. Since the advective time scale is determined by the PV ratio of the two vortices, the temporal resolution is given by $0.05 \div \frac{PV_{ETH}}{PV_{jet}}$ time units.

Recalling that one time unit in the model corresponds to one day, this means that for the experiments with a PV ratio of 2.5 for example, the temporal resolution is approximately half an hour.

Initial distance between the two vortices is the same for all experiments and is taken to be approximately two Rossby radius of deformation ($\simeq 2000km$) between the interfaces of the two vortices. This is equivalent to around $15°$ latitude so that for a polar vortex situated at $45°N$, the hurricane is initially at around $30°N$.

In summary, the specifications of the experiments are:

- spatial resolution of 256 even azimuthal intervals and 128 uneven radial intervals, equivalent to $\Delta\theta = 11km$, $\Delta r = 7km$ near the polar jet
- temporal resolution of five percent the advective time scale, equivalent to $0.05 \div \frac{PV_{ETH}}{PV_{jet}} days$
- radius of the polar jet is fixed at $4500km$
- distance between interfaces is two Rossby radius of deformation
- nine experiments with different values of PV ratio and ETH radius as tabulated in table 4.1

In passing, we remark that the model we are using for numerical experiments is quasi-geostrophic. Fundamental understanding of atmospheric and oceanic midlatitude dynamics was made possible through the simplicity of the quasi-geostrophic theory. Derived as a leading order theory in an expansion of the primitive equations, quasi-geostrophy holds for motions whose time scales are long compared to $f^{-}1$ (*Pedlosky*, 1987). For such motions the Rossby number $R_0 = \frac{U}{fL}$ is small, typically $\sim O(0.1)$. However, when the motion is

Table 4.1: The nine experiments performed for different flow settings.

	$\frac{PV_{ETH}}{PV_{jet}} = 1.0$	$\frac{PV_{ETH}}{PV_{jet}} = 2.5$	$\frac{PV_{ETH}}{PV_{jet}} = 4.0$
$R_{ETH} = 300km$	exp-1	exp-2	exp-3
$R_{ETH} = 500km$	exp-4	exp-5	exp-6
$R_{ETH} = 700km$	exp-7	exp-8	exp-9

very intense, as it is in the vicinity of rapidly rotating large scale vortices, the quasi-geostrophic approximation may break down locally. In our simulation, where strong ETH is considered and the strong polar jet frequently becomes severely curved, some regions are characterized by large Rossby number ($\sim O(1)$) and quasi-geostrophy may locally lose its validity. Nevertheless, it has been noted (*Keyser et al.*, 1992; *McWilliams et al.*, 1986) that quasi-geostrophy remains qualitatively successful in observational and diagnostic studies of mid-latitude cyclones in a regime that stretches the bounds of its validity (i.e. $R_0 \sim O(0.1) - O(1)$), indicating that the restriction may be less restrictive than it was thought to be. For this reason we argue that using a quasi-geostrophic model to simulate the interaction between two strong vortices such as the polar vortex and the ETH is not paradoxical despite the questionable applicability of the quasi-geostrophic equations. In our study, it appears that the barotropic dynamics of the interactions are well captured by the mechanistic model.

4.2 Numerical experiments

Figures 4.1 through 4.18 depict snap shots of the interaction between the polar jet and the ETH through a period of seventeen days, for the flow settings specified in table 4.1. The following is a discussion of the ETH-polar jet interaction based on the results shown in these figures.

Experiments 1 (figures 4.1 and 4.2), 4 (figures 4.7 and 4.8) and 7 (figures 4.13 and 4.14) present the interaction for a PV ratio of 1 and ETH radius of $300km$, $500km$ and $700km$ respectively (see table 4.1). In the course of seventeen days, these experiments indicate similar interaction pattern. The polar vortex only slightly deforms due to the relatively weak meridional velocity component attributable to the ETH forcing. The response is quasi-linear – no contour folding or wavebreaking is exhibited by the polar vortex interface. Moreover, the influence of the polar vortex's induced wave train on the latitudinal movement of the ETH is relatively small due to the wave train's small amplitude. On the other hand, the ETH is being strained by the polar jet. A thin filament of vorticity is drawn from the ETH and wrapped around the polar vortex. The ETH becomes smaller while the polar jet maintains its original size. The breaking of the filamentary vorticity from the ETH is attributed to the surgery procedure (as has been remarked in Subsection 3.1.3). Without surgery, the filament would stay connected to the ETH. However, *Dritschel and Waugh* (1992) claim that it would be so thin that the smallest amount of real flow dissipation would be required to break it. In Experiment 1, the breaking occurs on the eighth day. The ETH then appears to stop losing vorticity and regain a somewhat circular shape before an additional straining follows on the fourteenth day. As more and more vorticity is removed from the ETH, it is almost completely "dissipated" by the seventeenth day. *Dritschel and Waugh* (1992) have termed this regime "complete straining-out". For Experiments 2 and 3, the breaking of the filament occurs at about the same times and an additional straining follows later. As substantial vorticity lost by the ETH is apparent in all three experiments, the ETH of Experiment 1 is almost non-existent after seventeen days while the initially larger ETH of Experiment 7 is still fairly large (approximately

$500km$). Although the interaction pattern itself remains similar for these three experiments some differences can be noted. First, the deformation of the vortex appears to be stronger (i.e. larger amplitudes for the induced Rossby waves) for larger ETH as can be expected. Second, formation of a ridge-trough pattern to the east of the ETH becomes evident for the experiment with the large ETH during the initial stages of the interaction (up to the fourth day). This pattern does not appear in the small ETH experiment and it is only slightly detectable in the medium size ETH experiment. However, the pattern becomes disorganized as the PV filament becomes disconnected from the ETH. In the discussion of the next set of experiments, we shall encounter different evolution of the above mentioned ridge-trough to the east of the ETH.

Comparison between Experiments 1, 2 (figures 4.3 and 4.4) and 3 (figures 4.5 and 4.6), with similar ETH radius but various PV ratios (1, 2.5 and 4 respectively), reveals two interesting results. First, the stronger the PV of the ETH, the more able it is to maintain its circular shape in the presence of the induced shear flow of the polar jet. In other words, the ETH in Experiments 2 and 3 (at the stages prior to the merger of the ETH inside the polar jet) did not seem to undergo major distortion as in Experiment 1. Second, with the increase of the PV ratio from 1 (Experiment 1) to 2.5 (Experiment 2), the nature of the interaction changes. The interaction enters a nonlinear regime [1] where the polar vortex undergoes a more vigorous deformation and the ETH is merged into the polar vortex. Experiments 2 and 3 present similar interaction patterns. In Experiment 2, the Rossby wave train is generated by the ETH with a trough forming slightly upstream of the ETH location and a distinct ridge-trough pattern appearing to the east of it. The upstream

[1] When wavebreaking occurs, the reaction can no longer be considered linear, and thus the term nonlinear.

trough's amplitude gradually increases till day thirteen. A day later, it is becoming irreversibly deformed as it rolls up around the ETH. The ETH then merged into the polar vortex. At the same time, the trough east of the ETH intensifies as it narrows and reaches the lower latitudes. Its axis takes on a northeast-southwest orientation. The trough gradually becomes more filamentary as it continues to stretch and at later stages (not shown) it becomes a PV filament and is being cut off (by surgery) from the polar vortex. The stronger ETH of Experiment 3 further pushes the interaction into an even more nonlinear regime. Experiments 2 and 3 initially exhibit similar pattern only that the upstream trough starts to roll up around the ETH slightly earlier and a larger amplitude trough seems to form to the east. However, the later evolution of the trough is not the same and this is where the two regimes differ. The trough in Experiment 3 becomes narrow at its base but instead of evolving into a thin PV filament as it did in experiment 2, it broadens at its tip and subsequently evolves into a secondary cyclone (the size of the initial ETH but with PV equivalent to the polar vortex's) that is being cut off from the polar vortex (not shown). Consequently, the polar vortex decreases in size.

Experiments 5 (figures 4.9 and 4.10),6 (figures 4.11 and 4.12), 8 (figures 4.15 and 4.16) and 9 (figures 4.17 and 4.18) present a qualitatively similar interaction pattern as Experiment 3 and are thus grouped in the same regime. Some additional points are to be noted. The size of the secondary cut off low seems to be sensitive to the size of the initial disturbing ETH. When comparing Experiments 5 and 6 (with similar ETH radius but different PV ratio), the size of the secondary low which emerges from the jet is only slightly larger in Experiment 6 than it is in Experiment 5. On the other hand, comparison between Experiments 5 and 8 (with similar PV ratio but different ETH radius) reveals that the secondary low's size increases dramatically for the larger initial ETH. The same is true when comparison is made between Experiments 6 and 9. Another interesting observation is that for Experiments 5, 6 and 8, the stages of the interaction occur at approximately the same time. On the other hand, Experiment 9 shows a much more rapid development while the development in Experiment 3 is slower.

4.3 Discussion

All experiments support the hypothesis of the influence of an adjucent ETH on the polar jet through "action at a distance". The nature of the interaction is classified into three regimes. We define a regime here as a topologically different configuration of the vortices that is maintained at least for the duration of the experiment. The regimes are:

- regime A
  - Experiments 1, 4 and 7
  - weak response on the polar jet
  - ETH is being strained out.
- regime B
  - Experiment 2
  - formation of a Rossby wave train (trough upstream of the ETH position and a following ridge-trough pattern downstream)
  - ETH is wrapped up by the upstream trough and merged into the polar vortex

  - downstream trough becomes filamentary and is removed from the polar vortex

- regime C
  - Experiment 3, 5, 6, 8 and 9
  - formation of a Rossby wave train (trough upstream of the ETH position and a following ridge-trough pattern downstream)
  - ETH is wrapped up by the upstream trough and merged into the polar vortex
  - downstream trough becomes thin at its base but roll up into a cyclone at its tip, which is eventually being removed from the polar vortex

Our results should be viewed as qualitatively valid only because of the limitation in using a mechanistic model and a highly simplified idealized setting. Moreover, in the real case the hurricane's intensity changes as it wanders into higher latitudes (its radius increases and its maximum wind decreases) due to changes in the environment. We are unable to incorporate such changes into the numerical experiments. Nevertheless, some aspects of the idealized study are found to be in agreement with the observed phenomenon (reviewed in Chapter 2). The model proved to be robust in the sense that it captures well the dispersion of Rossby wave energy on the PV gradients of the polar jet and the formation of a wave train (trough upstream of the cyclone's position and a downstream ridge-trough pattern). Furthermore, the model was also able to retain the extraction of high PV (stratospheric) air from the polar vortex into low latitudes through an elongated north-east south-west tilted trough and the subsequent formation of a secondary cyclone (TUTT cell) which eventually becomes disconnected from the main vortex (see figures 4.18 and 2.1 for model simulation and the observed phenomenon respectively). The simulated straining of the hurricane was not observed in the results of Chapter 2 due to the inadequate resolution of the observed data. However, the hurricane's loss of symmetry as it moves into the mid-latitudes due to the environmental shear is well known in the literature.

To the best of knowledge, this is the first systematic study discussing the three different regimes found in the barotropic interaction of the ETH with the polar jet, a phenomenon found also in atmospheric analyzed datasets. It is worth to verify the existence of such regimes with additional cases and numerical experiments using a full fledge weather prediction model. Such study might serve as a future research goal but is outside the scope of this thesis.

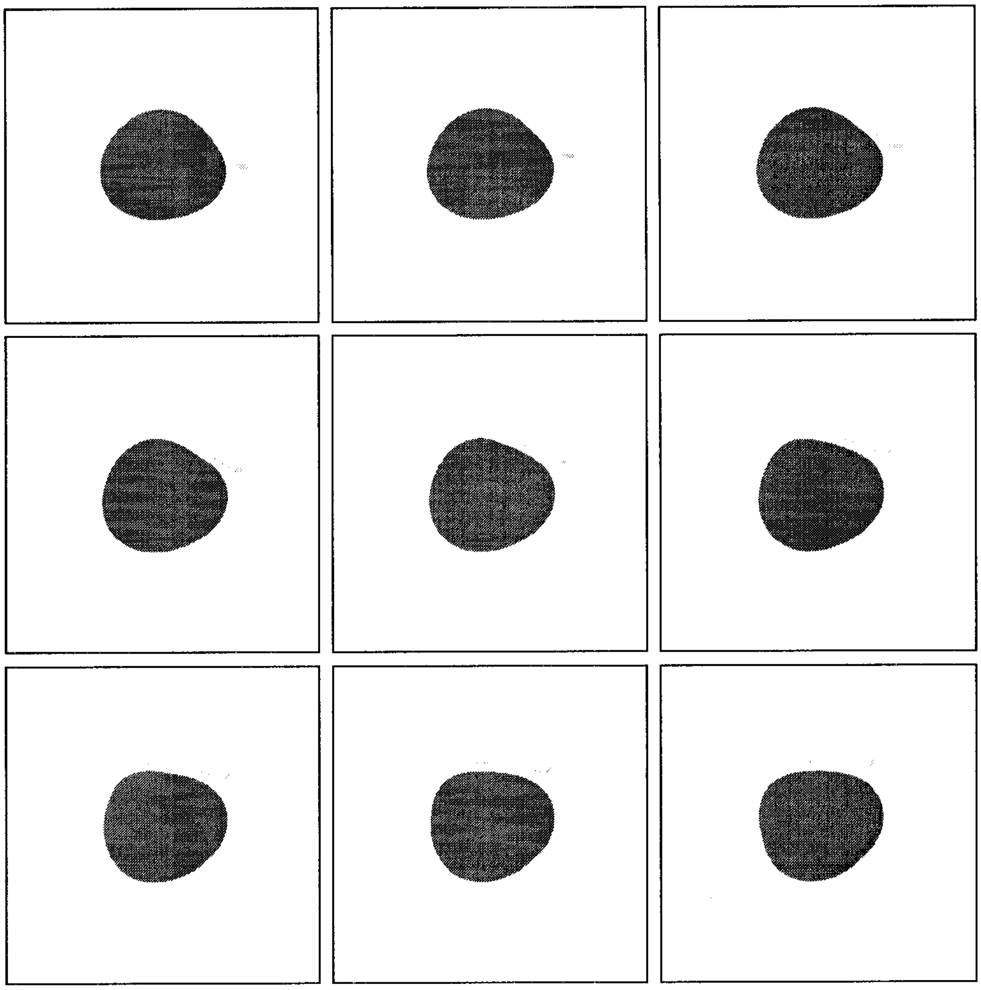

Figure 4.1: Simulation of the interaction between the polar jet (red PV patch) and the ETH (green PV patch) for ETH radius of 300 km and PV ratio of 1 (experiment 1). The frames run in time from left to right, and then from top to bottom, for t=0,1,2,3,4,5,6,7,8 days.

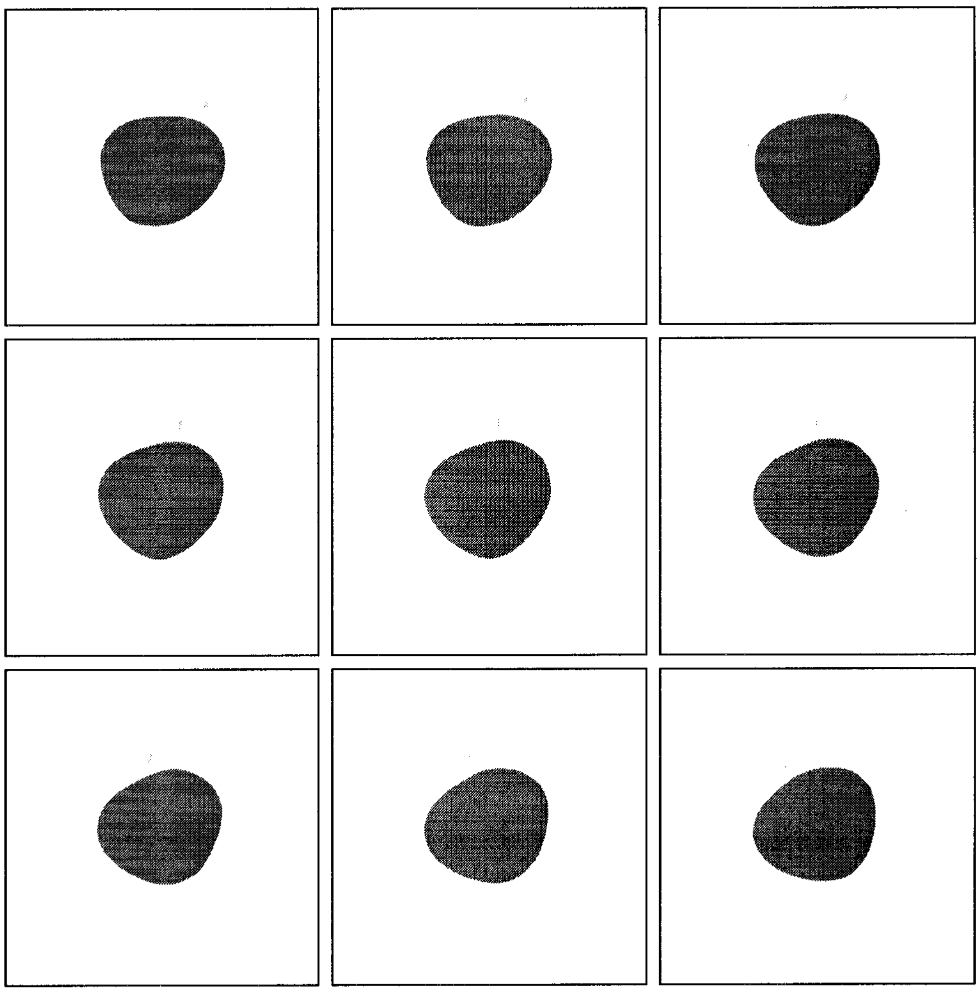

Figure 4.2: Continuation of figure 4.1 for t=9,10,11,12,13,14,15,16,17 days.

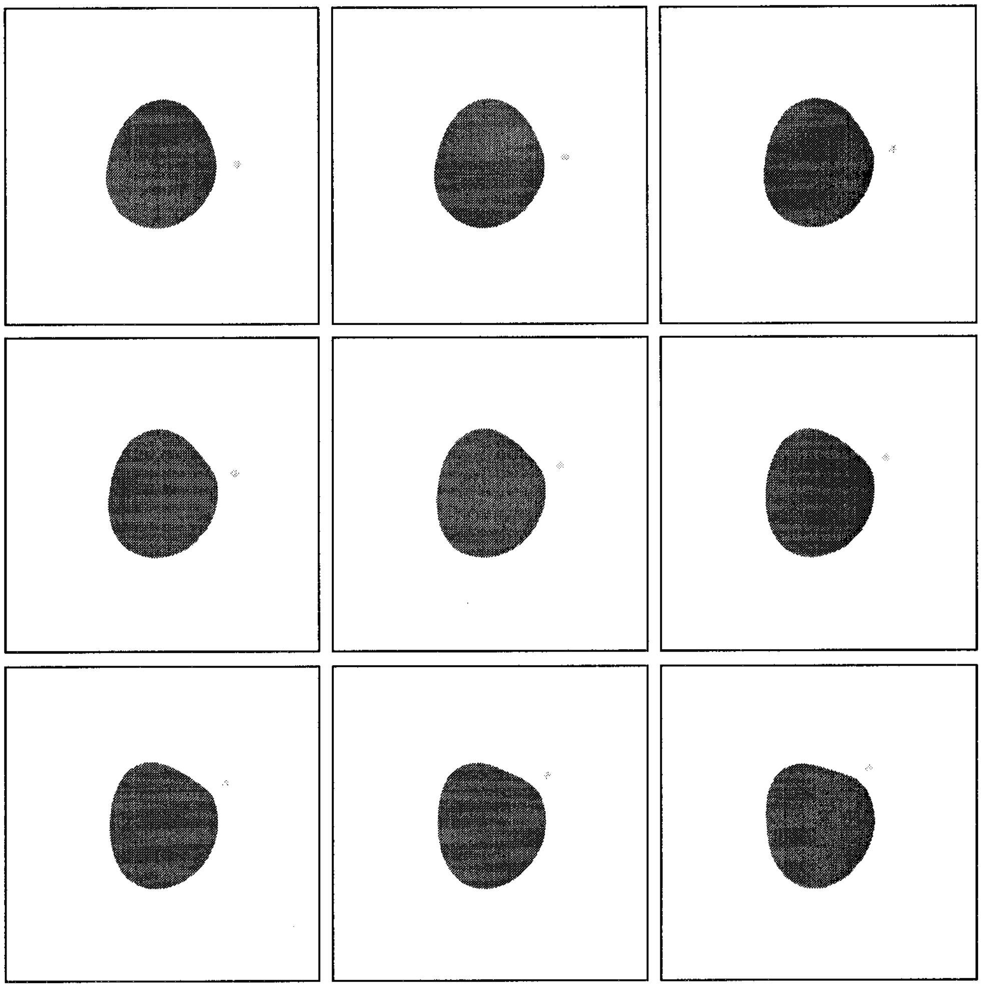

Figure 4.3: Simulation of the interaction between the polar jet (red PV patch) and the ETH (green PV patch) for ETH radius of 300 km and PV ratio of 2.5 (experiment 2). The frames run in time from left to right, and then from top to bottom, for t=0,1,2,3,4,5,6,7,8 days.

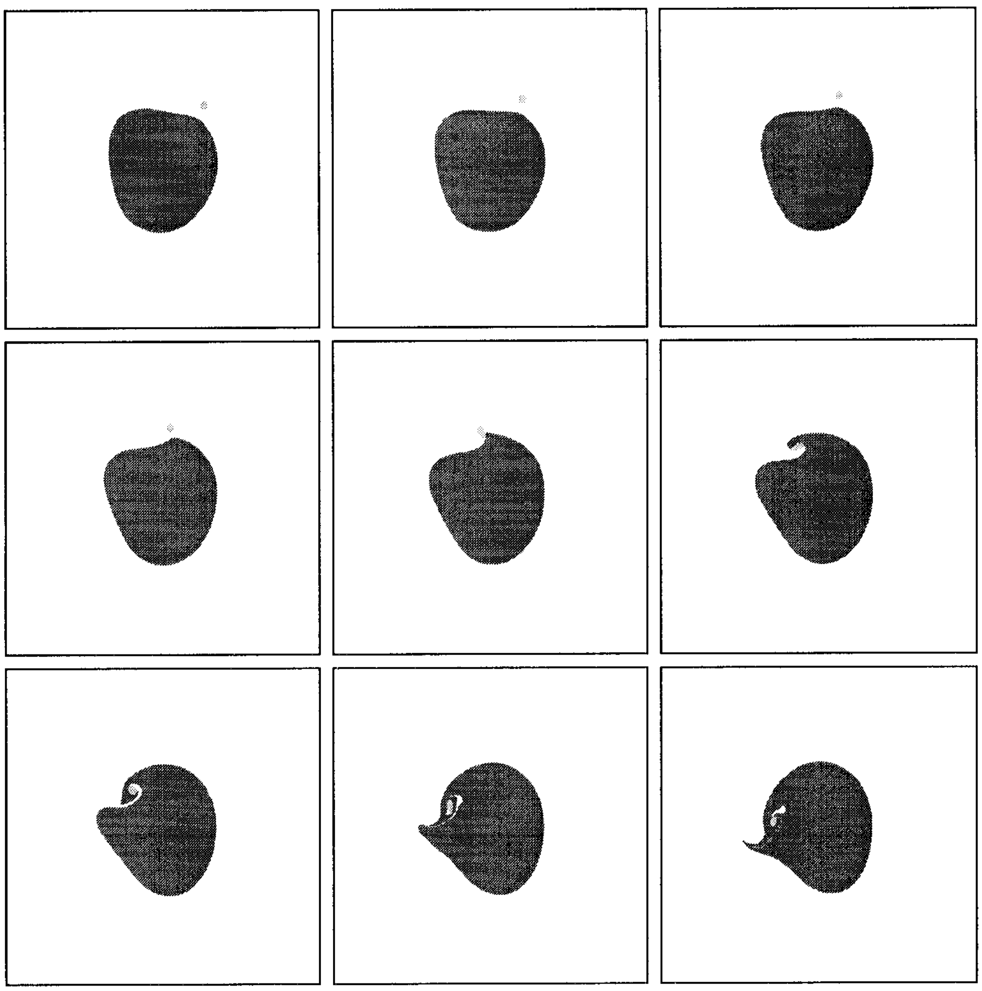

Figure 4.4: Continuation of figure 4.3 for t=9,10,11,12,13,14,15,16,17 days.

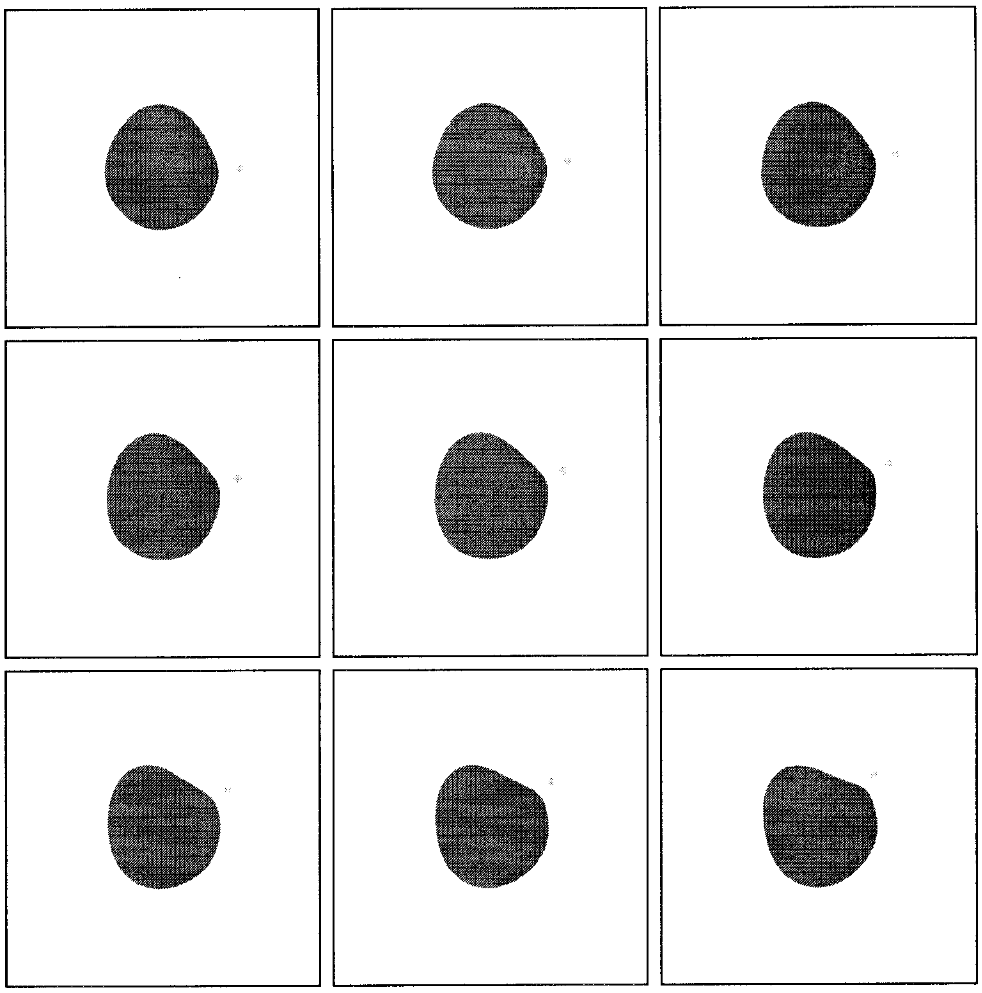

Figure 4.5: Simulation of the interaction between the polar jet (red PV patch) and the ETH (green PV patch) for ETH radius of 300 km and PV ratio of 4 (experiment 3). The frames run in time from left to right, and then from top to bottom, for t=0,1,2,3,4,5,6,7,8 days.

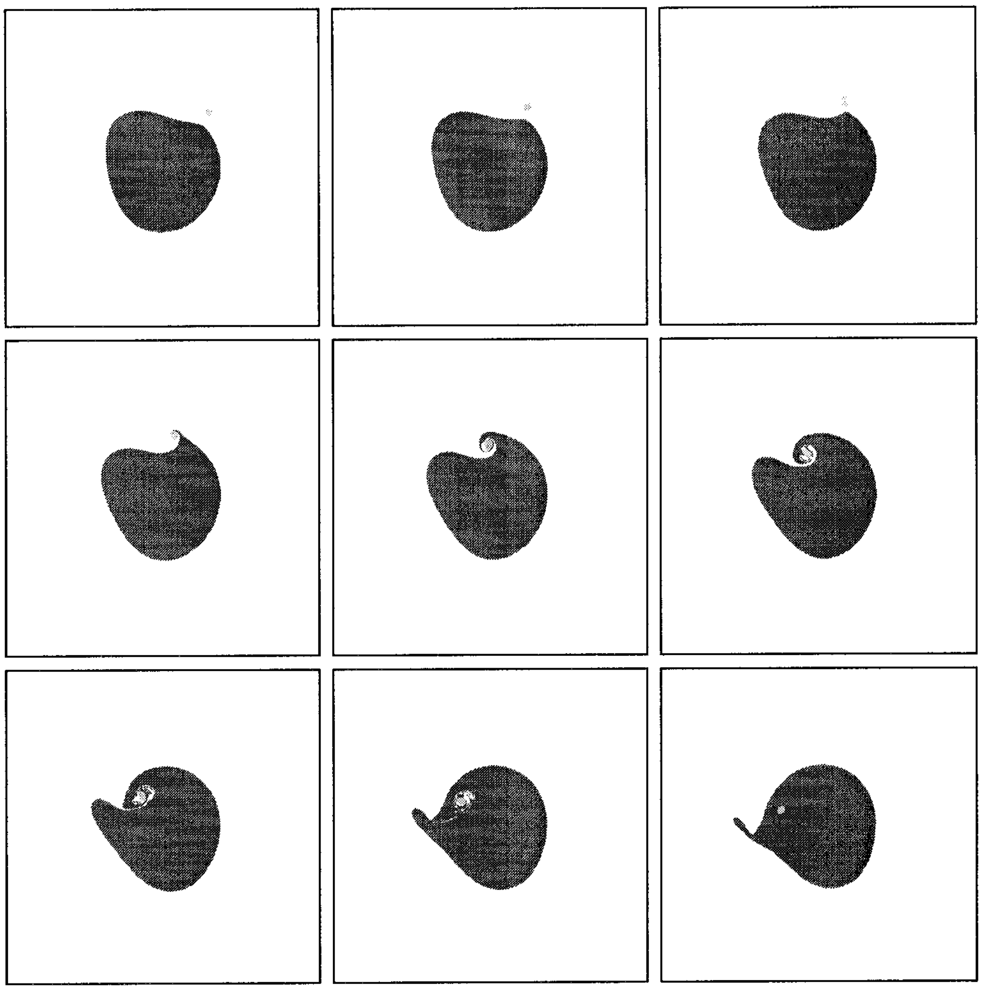

Figure 4.6: Continuation of figure 4.5 for t=9,10,11,12,13,14,15,16,17 days.

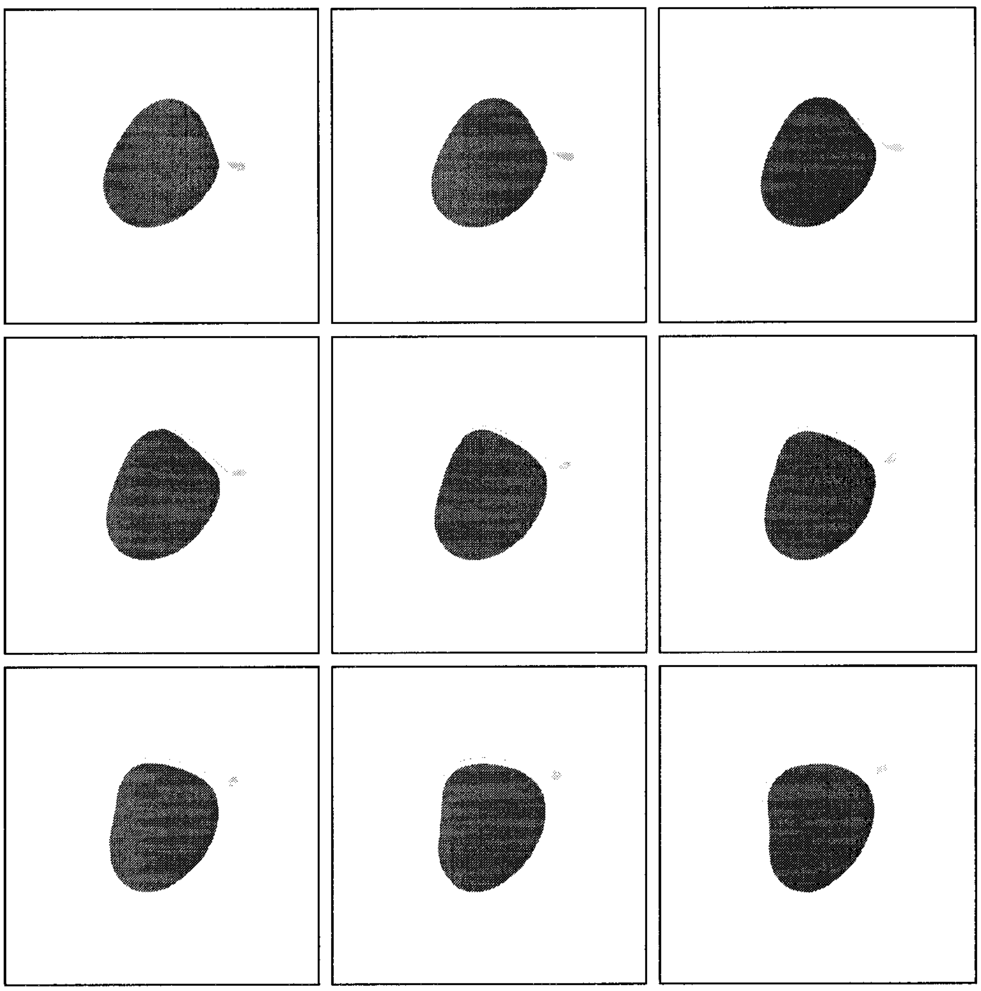

Figure 4.7: Simulation of the interaction between the polar jet (red PV patch) and the ETH (green PV patch) for ETH radius of 500 km and PV ratio of 1 (experiment 4). The frames run in time from left to right, and then from top to bottom, for t=0,1,2,3,4,5,6,7,8 days.

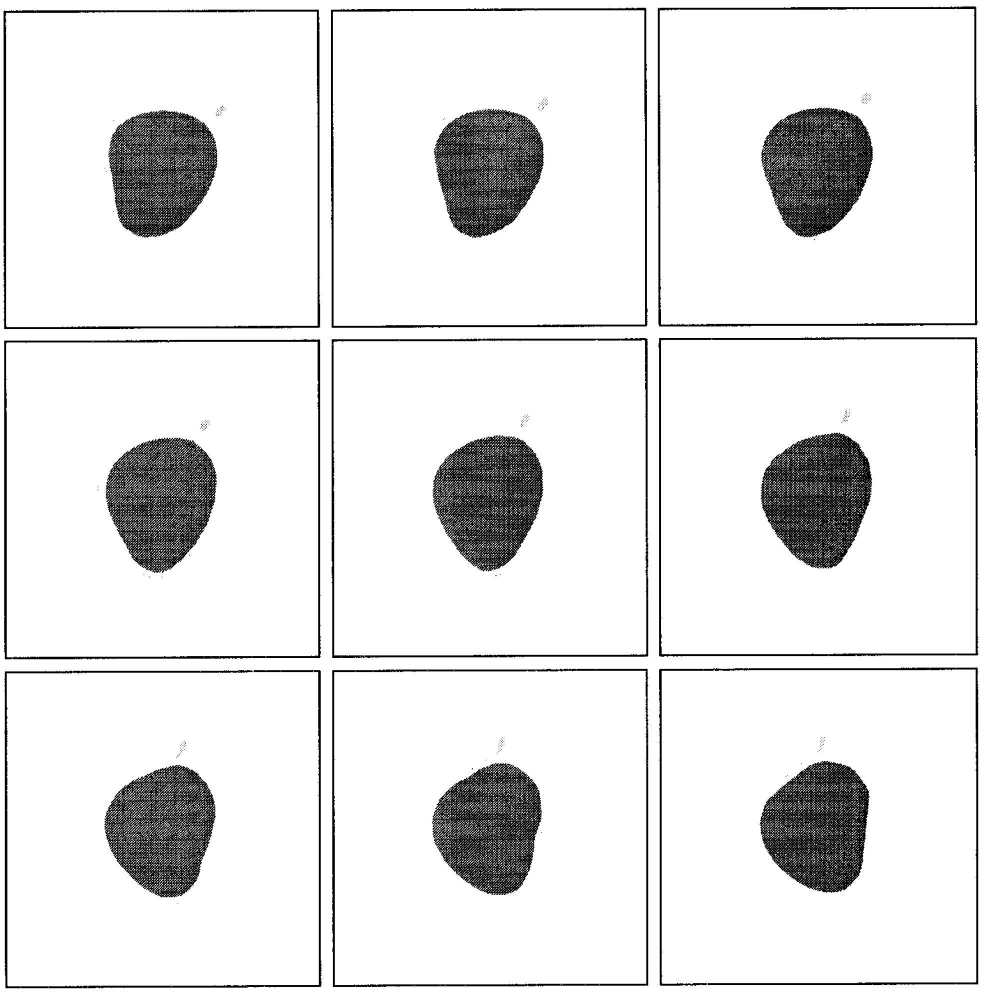

Figure 4.8: Continuation of figure 4.7 for t=9,10,11,12,13,14,15,16,17 days.

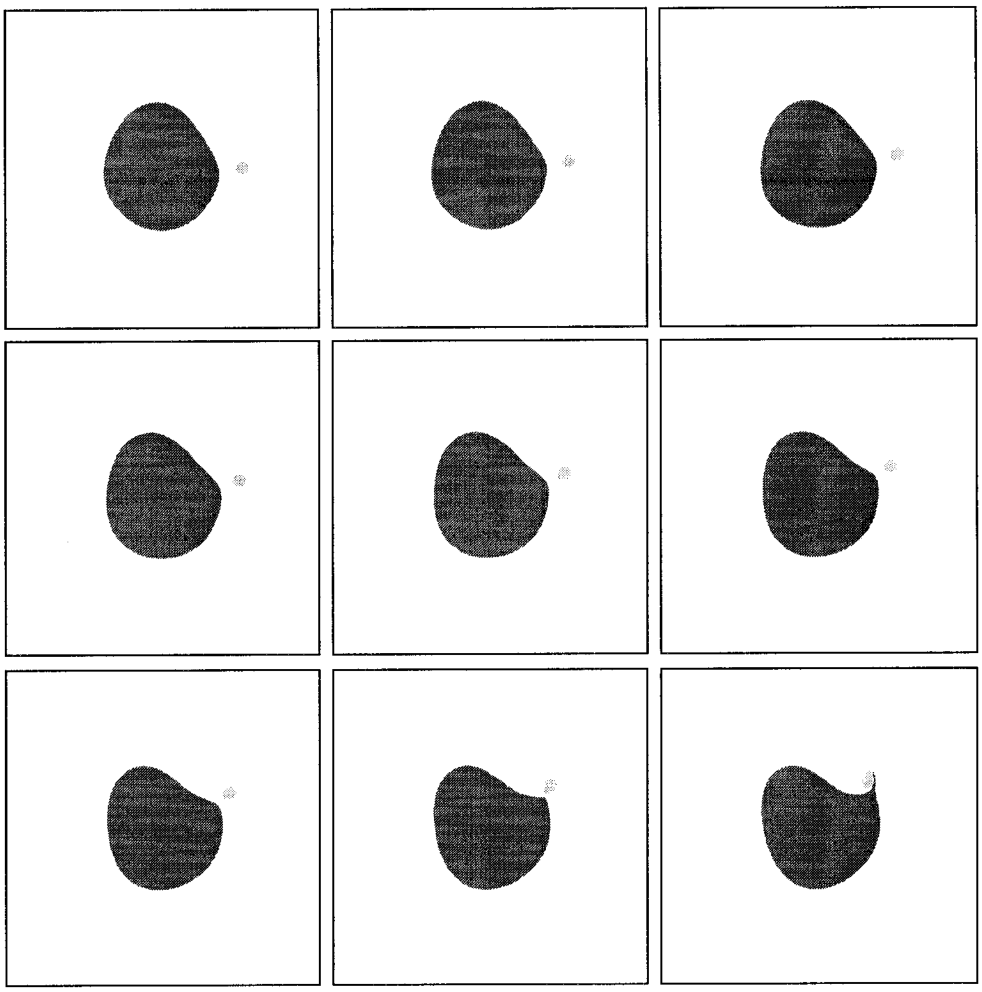

Figure 4.9: Simulation of the interaction between the polar jet (red PV patch) and the ETH (green PV patch) for ETH radius of 500 km and PV ratio of 2.5 (experiment 5). The frames run in time from left to right, and then from top to bottom, for t=0,1,2,3,4,5,6,7,8 days.

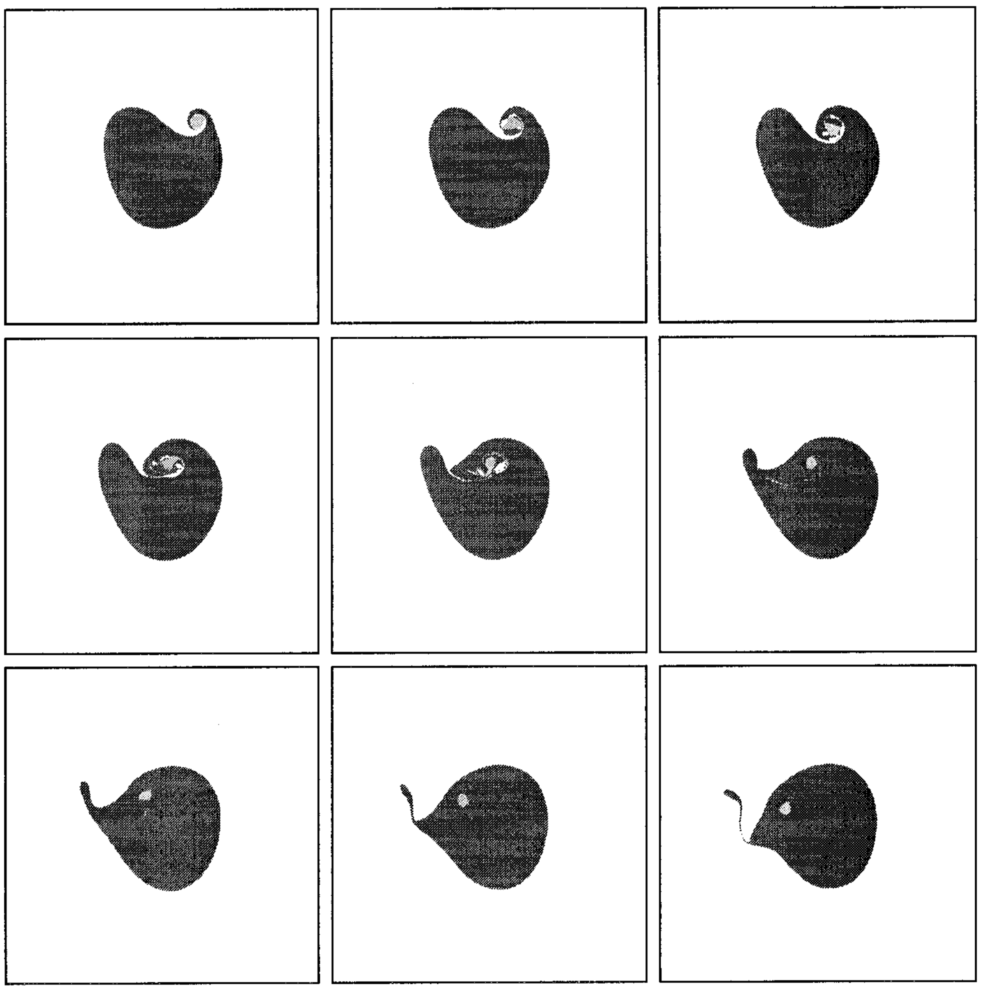

Figure 4.10: Continuation of figure 4.9 for t=9,10,11,12,13,14,15,16,17 days.

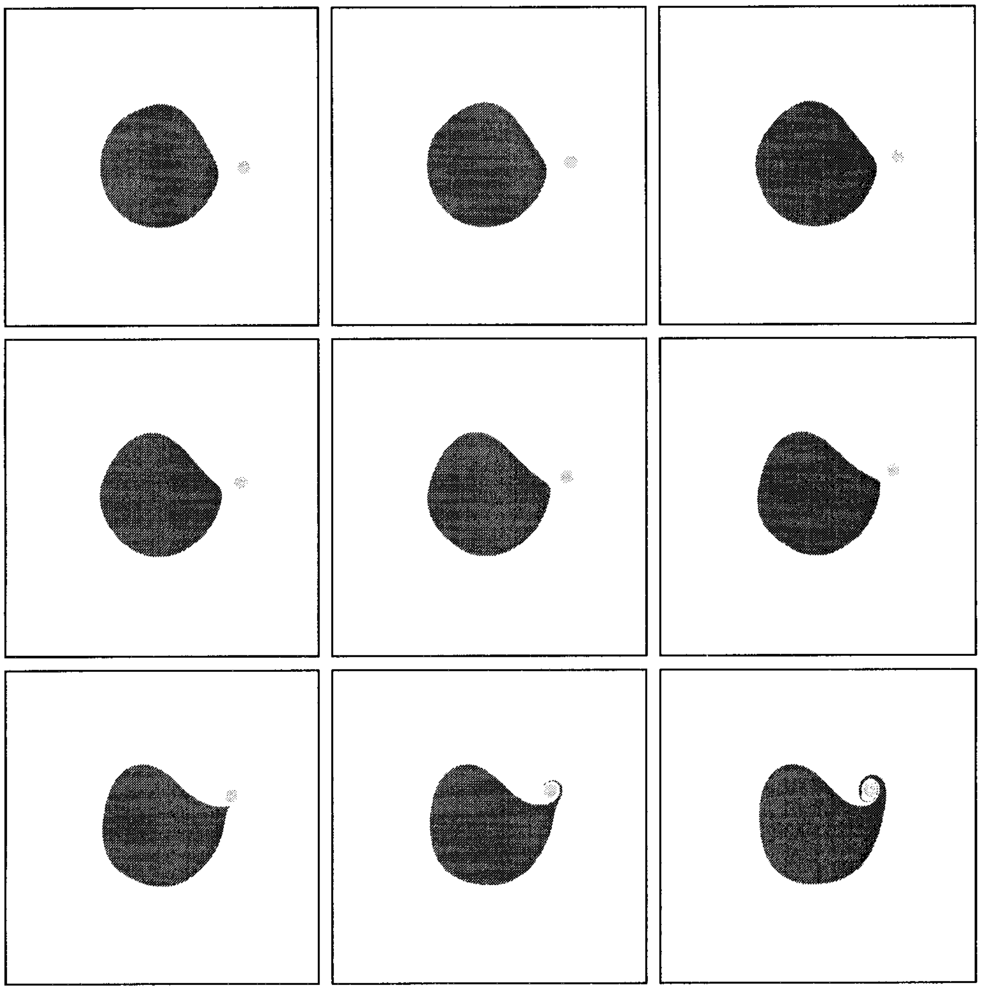

Figure 4.11: Simulation of the interaction between the polar jet (red PV patch) and the ETH (green PV patch) for ETH radius of 500 km and PV ratio of 4 (experiment 6). The frames run in time from left to right, and then from top to bottom, for t=0,1,2,3,4,5,6,7,8 days.

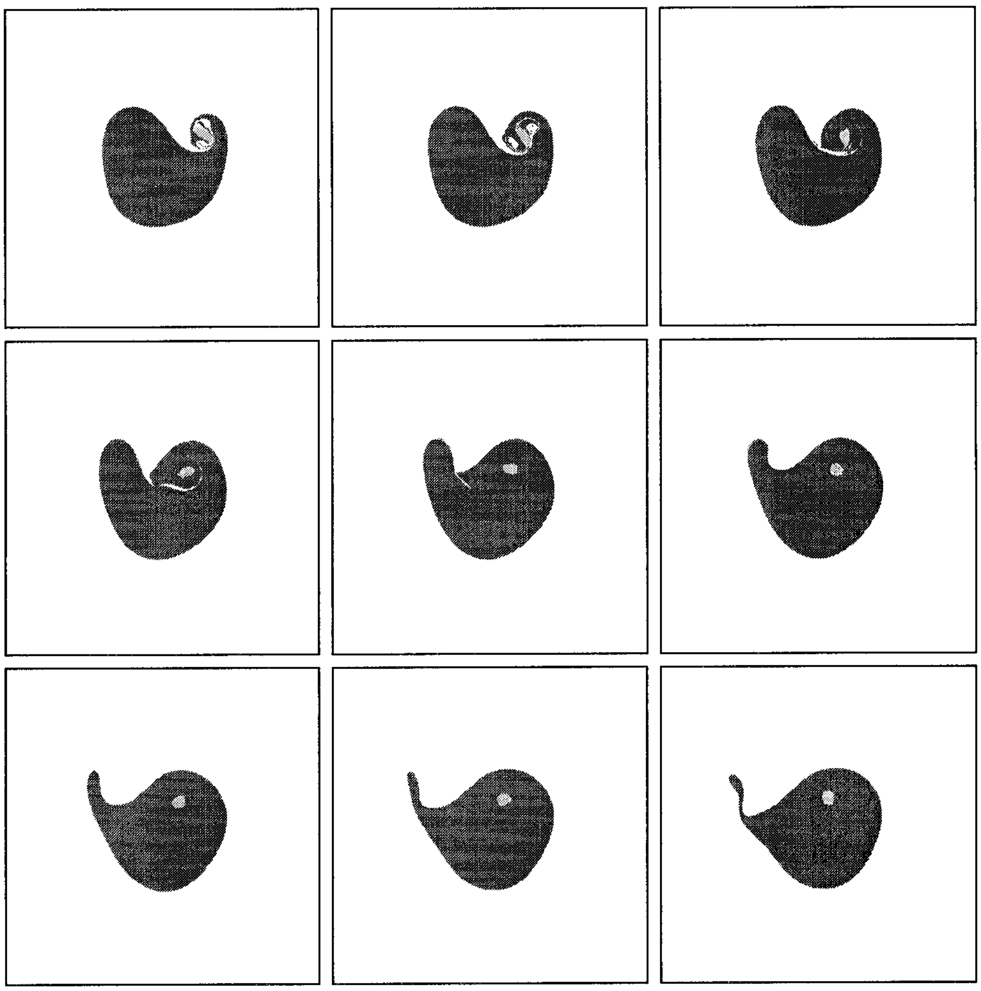

Figure 4.12: Continuation of figure 4.11 for t=9,10,11,12,13,14,15,16,17 days.

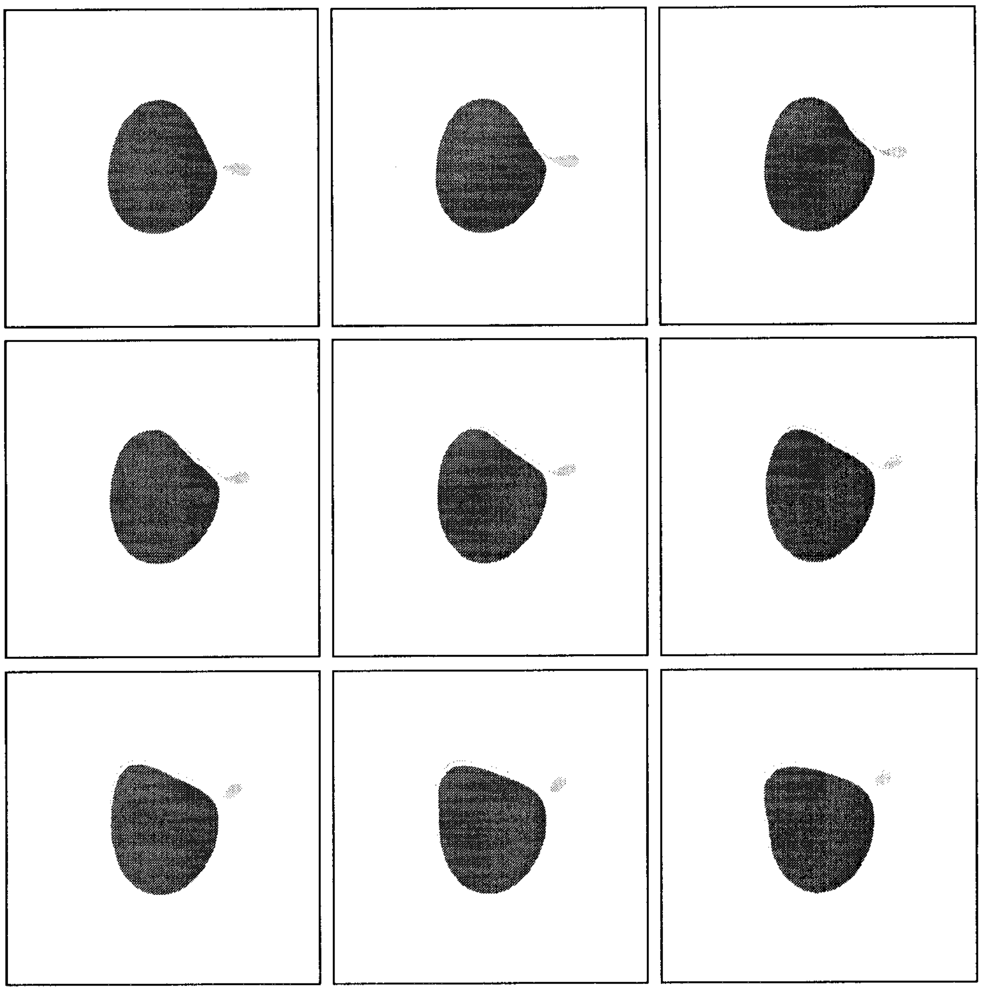

Figure 4.13: Simulation of the interaction between the polar jet (red PV patch) and the ETH (green PV patch) for ETH radius of 700 km and PV ratio of 1 (experiment 7). The frames run in time from left to right, and then from top to bottom, for t=0,1,2,3,4,5,6,7,8 days.

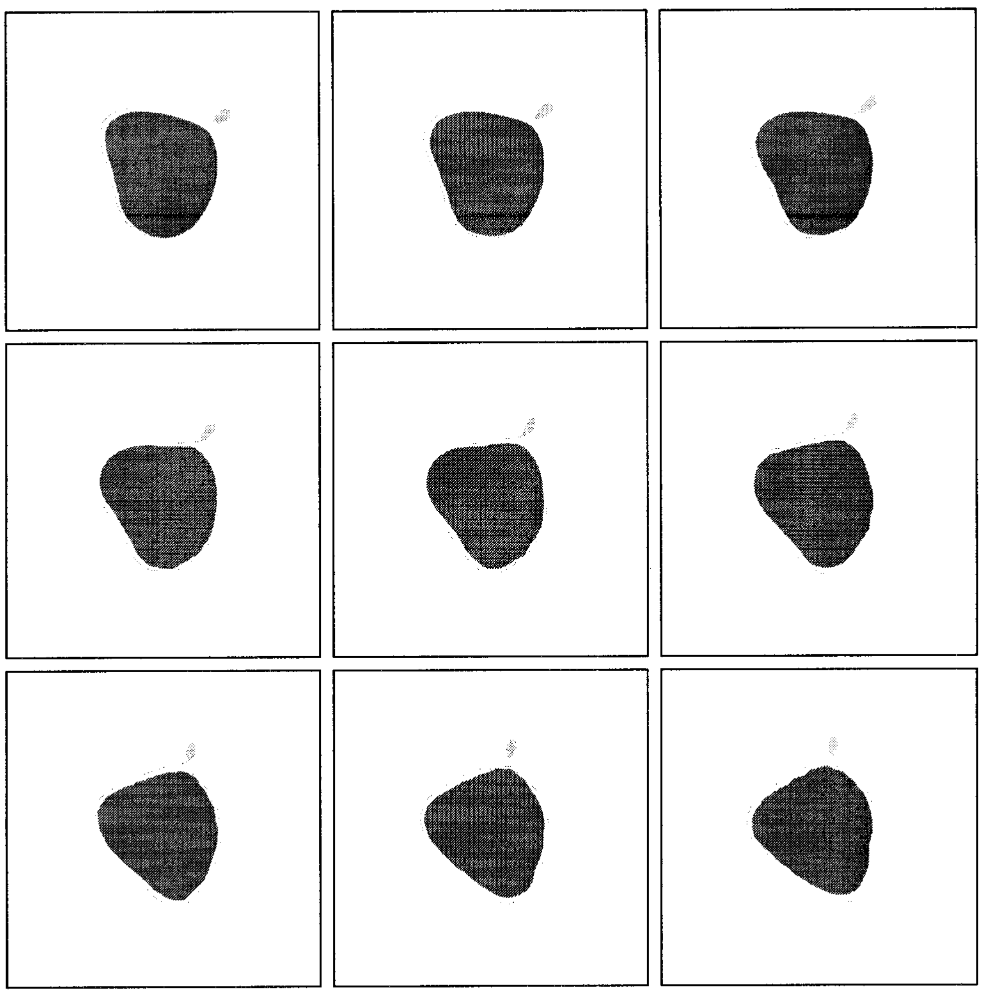

Figure 4.14: Continuation of figure 4.13 for t=9,10,11,12,13,14,15,16,17 days.

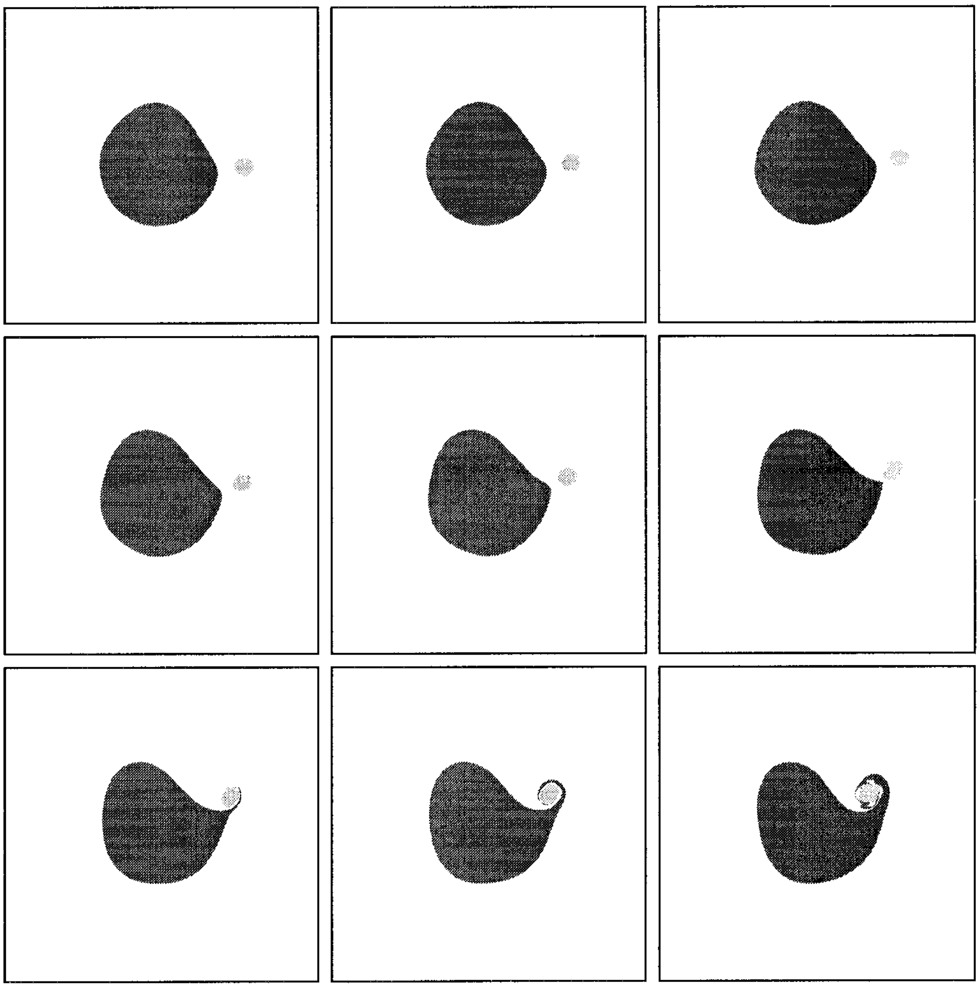

Figure 4.15: Simulation of the interaction between the polar jet (red PV patch) and the ETH (green PV patch) for ETH radius of 700 km and PV ratio of 2.5 (experiment 8). The frames run in time from left to right, and then from top to bottom, for t=0,1,2,3,4,5,6,7,8 days.

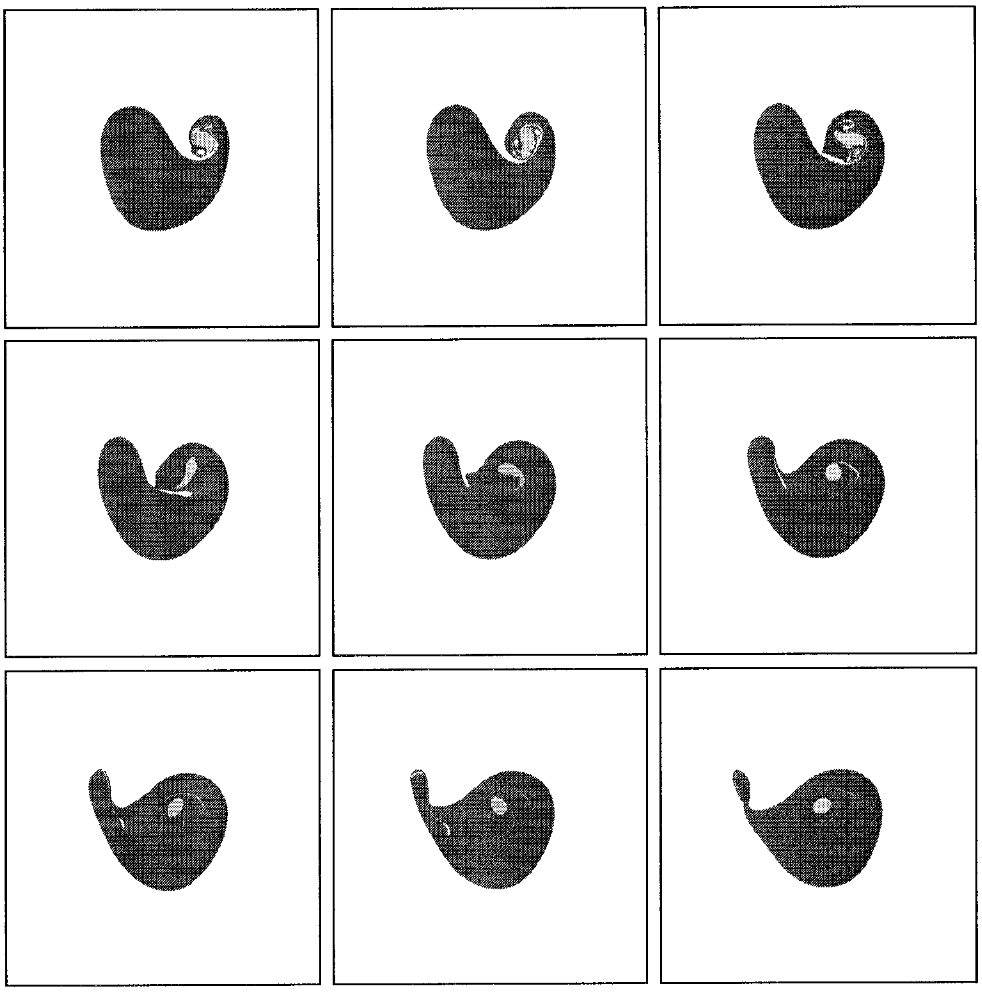

Figure 4.16: Continuation of figure 4.15 for t=9,10,11,12,13,14,15,16,17 days.

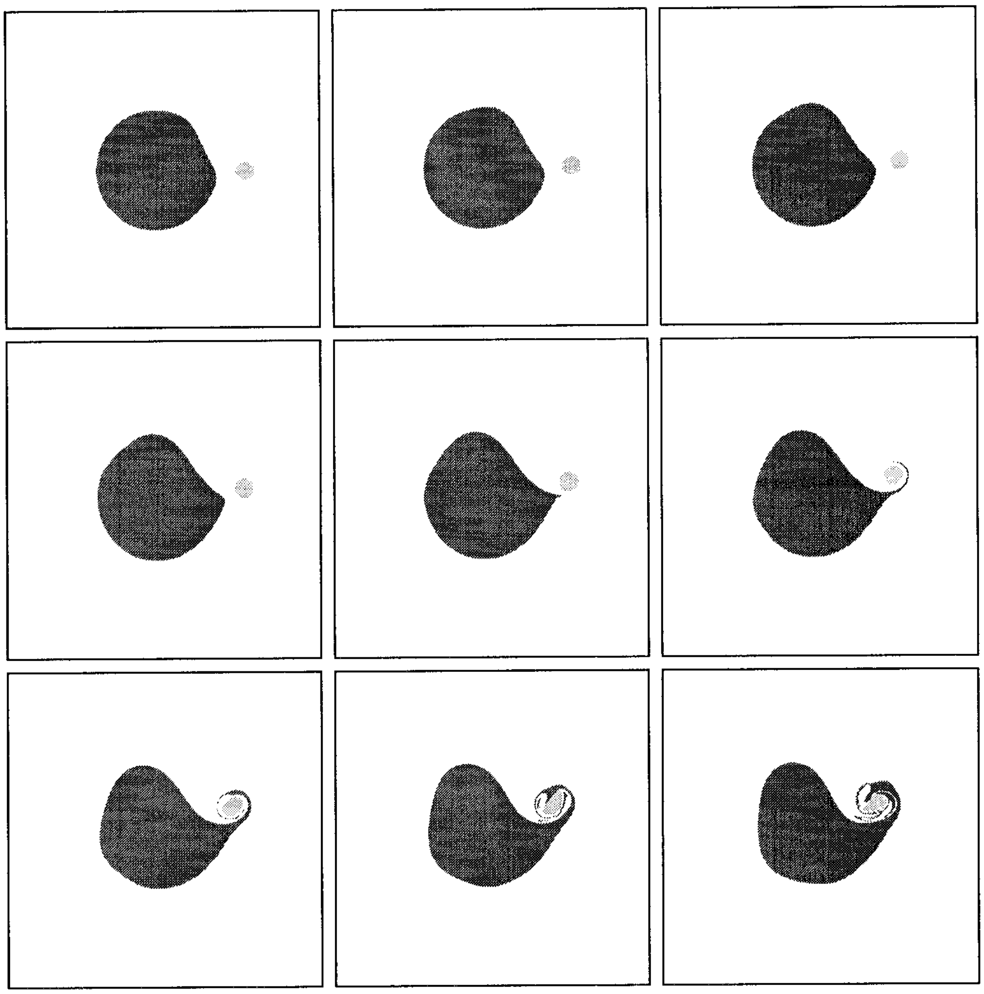

Figure 4.17: Simulation of the interaction between the polar jet (red PV patch) and the ETH (green PV patch) for ETH radius of 700 km and PV ratio of 4 (experiment 9). The frames run in time from left to right, and then from top to bottom, for t=0,1,2,3,4,5,6,7,8 days.

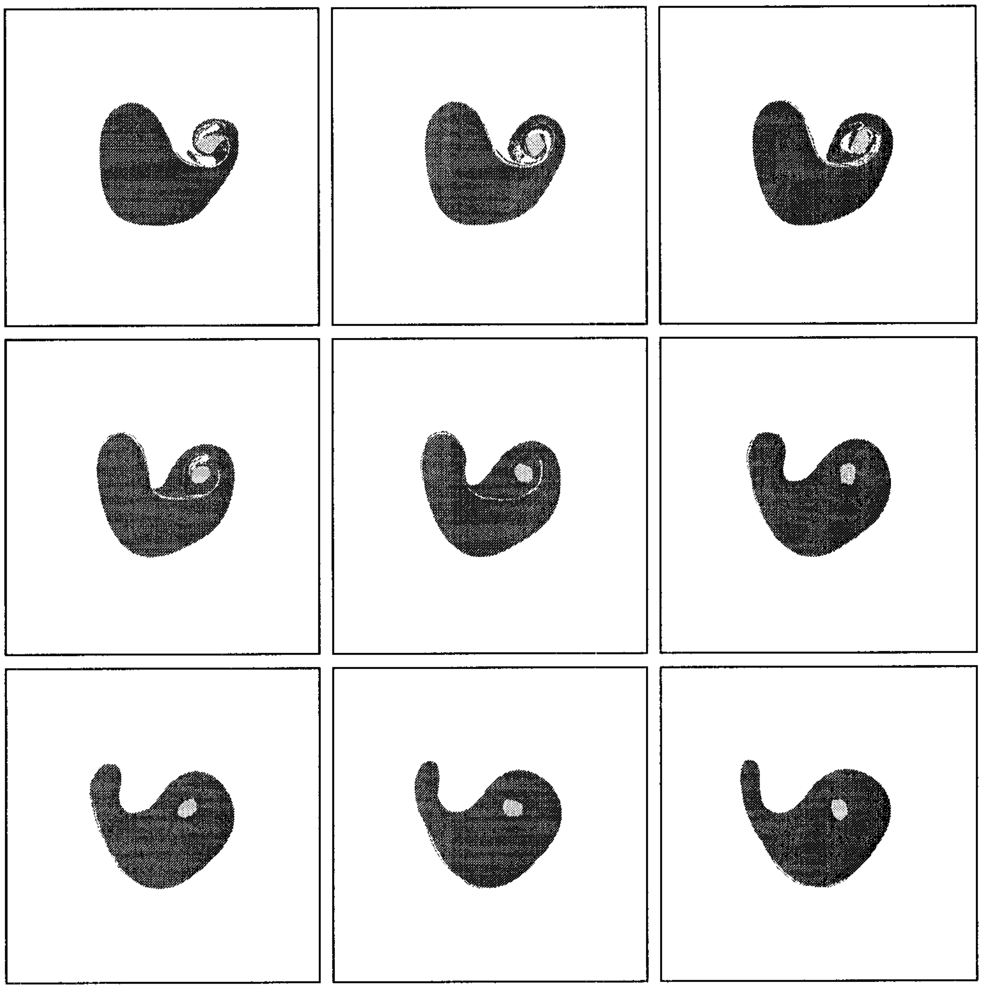

Figure 4.18: Continuation of figure 4.17 for t=9,10,11,12,13,14,15,16,17 days.

Chapter 5

Numerical experiments 2 - various resolutions

In Chapter 4 the dependence of the nature of the interaction on the cyclone's radius and PV was established. In this Chapter, sensitivity experiments on model resolution are performed to determine the relation between the intensity of the ETH and the skill of the Rossby wave prediction.

5.1 Specified parameters

The experiments in Chapter 4 have been conducted with very high spatial resolution of approximately 1280 uneven radial intervals and 2560 even azimuthal intervals (achieved by specifying 128 waves). In this Chapter, we re-run Experiments 5, 6 and 8 from Chapter 4. The parameters and flow setting described in Section 4.1 remained the same with the exception of one difference - coarser spatial resolution. We have decreased the resolution by a factor of two so that in the low resolution experiments (from now on Experiments 5*, 6* and 8*) there are approximately 640 uneven radial intervals and 1280 even azimuthal intervals (achieved by specifying 64 waves). At the vicinity of the jet, these values correspond to $11km$ azimuthal interval and $7km$ radial interval for Experiments 5, 6 and 8 (for calculation see Section 4.1) versus $22km$ azimuthal interval and $14km$ radial interval for Experiments 5*, 6* and 8*. The high resolution experiments are now considered to be "the truth" and the error derived from the lower resolution experiments is calculated with respect to "the truth".

5.1.1 Error calculation

The error refers to the differences in the positions of the PV front which delineates the polar jet. Assuming the high resolution experiments in Chapter 4 to be "the truth", changes in the position of the PV front are to be expected when trying to simulate "the truth". Literally, the error refers to the sum of all non-intersecting parts of the area bounded by the PV front contour of "the truth" and of a comparison simulation as illustrated in figure 5.1.

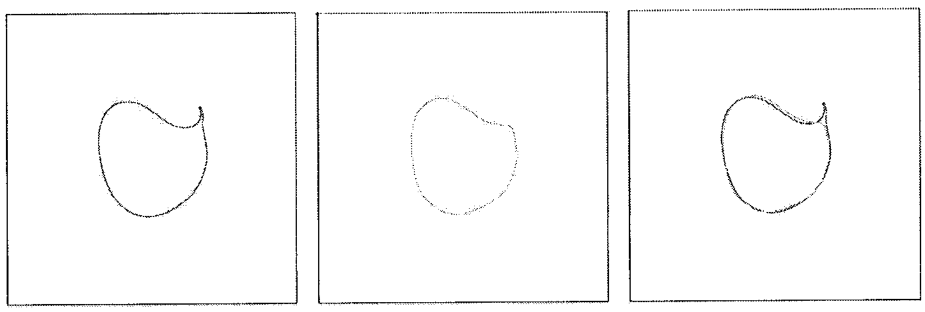

(a) (b) (c)

Figure 5.1: Demonstration of error calculation. The polar vortex contour on the eighth day for a) "the truth" as represented by Experiment 5 b) the simulation of "the truth" as represented by Experiment 5* c) demonstration of the error represented by the area bounded between the two contours

A simple algorithm was designed to calculate the difference areas. Detailed description of the algorithm appears in the appendix. Here, it suffices to note that the contour points are interpolated onto an equally spaced grid and the error is computed as the number of grid points in the non-intersecting areas. It is worth to note that the method we have used for calculation of the error is flexible in a sense that it can deal with greatly deformed contours such as the ones in our numerical experiments.

5.2 Numerical experiments

After applying the algorithm mentioned in Subsection 5.1.1, we end up with an error value (in term of number of grid points) for the simulation Experiments 5*, 6* and 8* with respect to "the truth" Experiments 5, 6 and 8. The error is plotted as a function of time for a period of six days (after which, surgery shears the polar vortex, multi contours are formed and calculation of the error is no longer appropriate after this stage). An exponential function is fitted to the error (using the least squares technique) with " T" being the e-folding time (in units of days). The "best fit" exponential error is shown in figure 5.2 and a discussion of the results follows.

5.3 Discussion

Examination of figure 5.2 reveals an interesting observation. It is clear that the more intense the cyclone is, the faster the error grows (characterized by a smaller e-folding time). In other words, it is harder to predict the response of the polar jet to a stronger perturbing cyclone than it is for a weaker one.

Operational forecast centers rely heavily on numerical models for issuing a weather forecast. Obviously, model resolution plays a major role in the accuracy of this forecast. The relatively small scale of a tropical cyclone makes numerical forecast even more problematic. Today's global forecast models' inability to properly capture a small scale phenomenon such as a hurricane (due to inadequate resolution) results in poor forecasting skill of Rossby wave excitation initiated by the same hurricane. *Shapiro and Thorpe* (2004) state that "forecast skill, as determined by the time at which the 500-mb anomaly correlation skill score falls below 60%, has advanced from 5 days

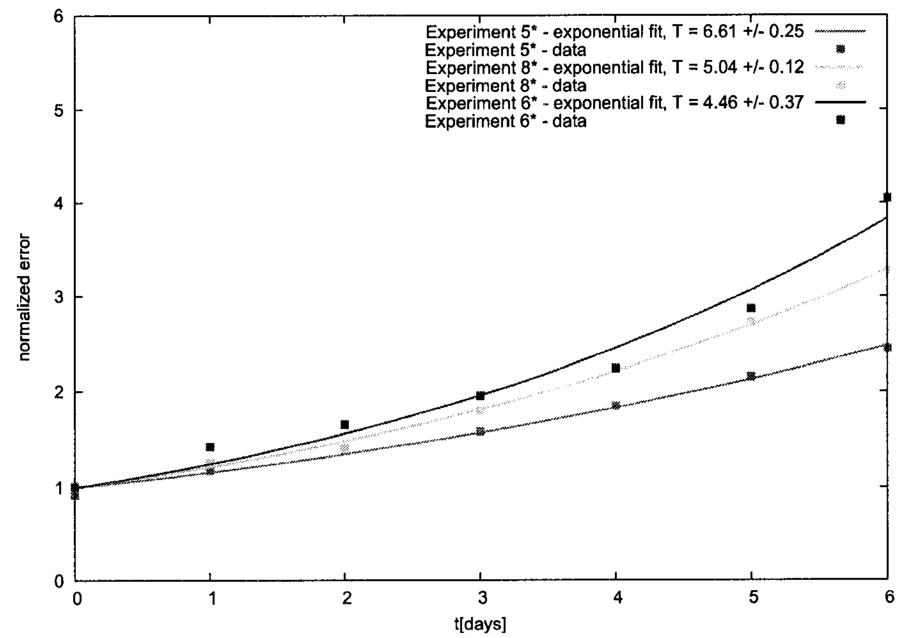

Figure 5.2: The error associated with the simulation of Experiments 5*, 6* and 8* with respect to "the truth" represented in Experiments 5, 6 and 8. The data points of the error are marked by filled squares and the exponential fit is represented by straight lines. The exponential fit of the error in this figure is normalized by the calculated value of the error at $t = 0$ to give $\epsilon/\epsilon(t = 0) = e^{(t/T)}$. The data points of the error are normalized by the same value. The associated e-folding time (+/− the uncertainty error) for each experiment appears at the upper right corner.

in 1980 to 8 days in 2003". The experiments conducted in this Chapter with a mechanistic model, similarly assuming that the forecast skill is determined by the error e-folding time, indicte a forecast skill which, at times (for example Experiment 8), falls to almost half of the currently accepted values (as reported by *Shapiro and Thorpe*, 2004). Keeping in mind that the experiments have been conducted under resolution which is equivalent to approximately a $22km * 14km$ grid box (finer than today's global numerical forecast models), the forecast skill could have turned out to be even poorer. Furthermore, between the best (Experiment 5) and the worst (Experiment 6) prediction, there is a decrease in predictability of more than thirty percent. Such a number gives us a good indication of how sensitive the prediction in regime C (see Chapter 4) really is.

Clearly, we should not attempt to draw a conclusive comparison between a comprehensive numerical forecast model and a mechanistic model. Nevertheless, the above mentioned results may be used to shed light on the importance of resolution improvement for a successive forecast of the phenomenon examined in the current research. Moreover, these results suggest that numerical weather prediction model resolution, which has increased systematically over the last few decades, probably still needs to be improved in order to adequately capture the interaction of the ETH with the polar jet.

Chapter 6

Conclusions

6.1 Thesis summary

The present study investigates the excitation of a Rossby wave train on the polar jet's enhanced potential vorticity gradients by an approaching hurricane through "action at a distance".

As a first step, three case studies were presented in order to demonstrate that the dispersion of Rossby wave energy and the formation of a Rossby wave train, initiated by a hurricane situated away from the jet, is indeed feasible. These cases reveal similar evolution pattern where a large pocket of stratospheric air is ejected from an initial zonally aligned polar vortex approximately 30° longitude east of the location of the hurricane. The initiation of the wave train in all three cases, depicted clearly through the Hövmoller diagrams in Chapter 2, occurred while the hurricane was situated about 30° latitude away from the jet. This confirms the validity of the "action at a distance" concept. The connection between the existence of a distant hurricane and the formation of a Rossby wave train has not been rigorously proven in Chapter 2 and remained hypothetic. Nevertheless, the existence of a hurricane at the same time of the Rossby wave initiation along with the increase in the wave train's amplitude concomitant to the decrease in the hurricane's intensity provide solid support for our assumption.

Despite the supporting evidence on the ability of the hurricane to excite Rossby waves, presented in Chapter 2, we were unable to distinguish between the adiabatic and the diabatic contributions and it was assumed that both processes potentially coexist. Chapter 4 was able to zoom in on the adiabatic interaction by demonstrating Rossby wave excitation on the polar jet by an approaching cyclone (ETH) in an idealized adiabatic setting of a mechanistic model (f plane, quasi-geostrophic, shallow water) based on the contour dynamics numerical method. In the model, the polar jet and the ETH are both represented initially by circular, positive PV patches at the same level. The radius of the polar jet is fixed at $4500km$ and nine experiments were conducted with different values of PV ratio ($\frac{PV_{ETH}}{PV_{jet}}$) and ETH radius. The initial distance between the two features is fixed to approximately two Rossby radius of deformation ($\simeq 2000km$) in all the experiments. The nature of the interaction as a function of the different settings (different values of PV ratio and ETH radius) was studied. It was shown that the characteristics of the interaction can be classified into three regimes. Regime A includes three experiments with a PV ratio of 1 and differing ETH radii of $300km$, $500km$ and $700km$ respectively. This regime yielded a weak response (shallow waves, no contour folding or wavebreaking) on the jet and an ETH which is being strained out by the jet's forcing. Regime B includes the experiment with a PV ratio of 2.5 and ETH radius of $300km$. This regime is marked by the formation of a Rossby wave train (trough upstream of the ETH position and a following ridge-trough pattern downstream) and an ETH which is being wrapped up by the upstream trough and merged into the polar vortex. The downstream trough becomes filamentary and is eventually removed from the polar vortex. Regime C includes the experiments with a PV ratio of 2.5 and ETH radius of $500km$ and $700km$ respectively as well as the experiment with a PV ratio of 4 and respective ETH radii of $300km$, $500km$ and $700km$. Regime C exhibits the same pattern of Rossby wave train but it differs from regime B in the behaviour of the downstream trough. Instead of becoming a thin filament as it did in regime B, it is becoming thin at its base but rolled up into a cyclone at its tip. This cyclone is eventually being removed from the polar vortex. The ETHs in regimes B and C do not seem to undergo any major distortion as those in regime A and are more or less able to maintain their circular shape prior to the merger with the polar jet. This suggests that the stronger the PV of the ETH, the less likely it is strained by the polar jet's forcing.

After the dependence of the nature of the interaction on the ETH's radius and PV anomaly was established in Chapter 4, we proceed to determine the effects of these parameters on the skill of predicting Rossby waves. We selected three experiments from Chapter 4 and re-run the same experiments with the exception of one difference – coarser spatial resolution. In fact, we have decreased the resolution by a factor of two. The higher resolution experiments were then considered to be "the truth" and the error of the lower resolution experiments was calculated relative to the position of the PV interface which delineates the polar jet. It was found that it is harder to predict the response of the polar jet to a stronger perturbing cyclone than for a weaker one. Furthermore, our results implied that the resolution in today's weather prediction models still needs to be improved in order to capture the ETH-polar jet interaction with sufficient accuracy.

6.2 Final remarks

To date, the interaction of a tropical storm with the mid-latitude PV gradients at upper level is frequently associated with substantial reduction in the skill of medium range forecast (*Jones et al.*, 2003). Perhaps one of the strongest examples of this goes back to 1987. In October that year, a severe low pressure system (with central pressure of 958mb!!!) hit England, produced hurricane force winds and was responsible to the deaths of over 20 people. This storm was considered by many as one of the worst storms in the history of the country. Reasons for the development of such an intense system were related to the jet stream coming from America in the wake of hurricane Floyd (*Hoskins and Berrisford*, 1988) and errors in the forecast were tracked back to the misrepresentation of the hurricane-jet interaction

(*Jones et al.*, 2003).

There is no question that an improved understanding of the interaction between a tropical storm and the upper level mid-latitude PV gradients is needed. The advantages of a contour dynamics model (and Dritschel's CASL model in particular) for the understanding of the adiabatic aspects of the interaction are well summarized in Section 1.4 and in Chapter 3. A future research opportunity might involve a slightly more realistic setting where inter-level interaction are also considered. Such option is available in the CASL model. Comprehensive outlook of both the adiabatic and the diabatic aspects of the interaction might only be available through well designed integration of simple and full physics models.

Appendix

The following is a detailed description of the algorithm designed for calculation of the error in Chapter 5.

The location of the PV front contour is given in the model by a series of points (x, y), distributed irregularly on a circular domain with a radius of 1. In order to design an algorithm which calculates the error, the points should be interpolated onto a regular grid. This is *stage A* of the algorithm. An equally spaced square grid of 4,000,000 points was chosen (2000*2000) and the x and y values of each point (which were given with a precision of six figures after the decimal point) were multiplied by 1000 and were then rounded to the nearest integer. Now that the contour's points were "placed" on a regular grid, we next have to make sure that the imaginary contour line which connects all the points would be represented in every line on the grid (but not necessarily in every column). This forms *stage B* of the algorithm. The parameters of a straight line passing through each two adjacent points is calculated and points are added on the grid (each time there was a grid line which is missing a point) with the constraint that they will lie as close as possible to this line. Figure 6.1 demonstrates how stage B works. The contour is initially represented by the red circles and a straight line is drawn between two adjacent points (see figure 6.1(a)). After the execution of stage B, the green "x" points are added (only when the straight line is not represented in a certain grid line) in a way that they are as close as possible to that line (see figure 6.1(b)). Eventually, the imaginary contour is now represented by points in every line on the grid but not necessarily in every column.

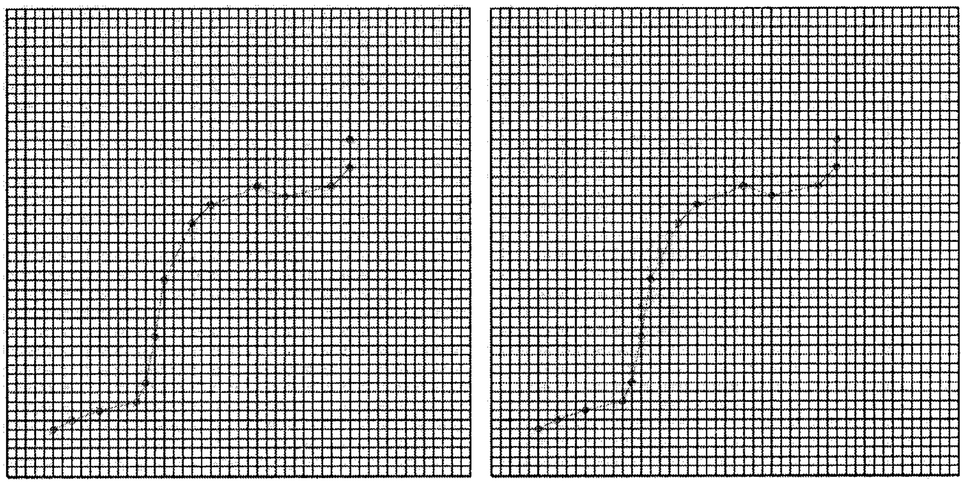

(a) (b)

Figure 6.1: Demonstration of how stage B works. a) the original contour points and the straight line passing through each two adjacent points b) the points added after the execution of stage B

In *stage C*, all the points (the original points and the points added after the execution of stage B) which belong to the contour were given a value of "1" and all the remaining grid points were given the value "0". In *stage D*, we assign a value of "1" to all the points which lie on the contour and inside the contour. For that, we have used the following method. Starting from top to bottom and from left to right, for each point of the grid with a value of "0", we travel through the rest of the line (to its right). If we crossed a "1" value point even number of times, the point was determined to be outside the contour and its value of "0" remaines unchanged. If we crossed an odd number of times, the point was determined to be inside the contour and its value was changed from "0" to "1". Care was taken for cases of corners (or local extremums) and continuous stretches of value of "1" points at the same grid line. The algorithm was adjusted accordingly in order to deal with such special cases. We have followed the same procedure (stage A through D) for both the contour which represents "the truth" and the contour which represents the simulation of "the truth". Figure 6.2 demonstrates how stage D works. Point "a" for example is determined to be outside the contour since a run on the rest of the line (to its right) will result in crossing the contour four times (even number). On the other hand, for point "b" it will cross the line only once (odd number) and as such, point "b" is determined to be inside the contour. Note that the actual grid we have used (2000*2000 points) is much finer than the grid presented in this figure. The grid in the figure is exaggerated only for clarity reasons.

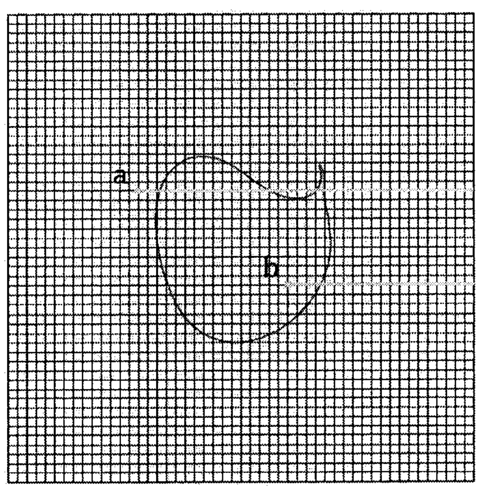

Figure 6.2: Demonstration of how stage D works.

Stage E is the last step in the algorithm where the calculation of the non-intersecting areas itself takes place. In this stage, we simply subtracted one filled contour from the other (since they are both on the same domain size) and count the number of points with values of either "1" or "-1". The error is given by the number of grid points in the non-intersecting areas.

Bibliography

Ambaum, M., and W. Verkley (1995), Orography in a contour dynamics model of large scale atmospheric flow, *Journal of Atmospheric Sciences*, *52*, 2643–2662.

Appenzeller, C., and H. C. Davies (1992), Structure of stratospheric intrusions into the tropopause, *Nature*, *358*, 570–572.

Bell, G. I. (1990), Interaction between vortices and waves in a simple model of geophysical flow, *Physics of Fluids*, *2A*, 575–586.

Bishop, C. H., and A. J. Thorpe (1994), Potential vorticity and the electrostatics analogy: Quasigeostrophic theory, *Quarterly Journal of the Royal Meteorological Society*, *120*, 713–731.

Blackburn, M., B. Hoskins, P. Inness, and J. Slingo (2003), 2002- a summer of floods and draughts, *Planet Earth*, *23*.

Chen, Y., G. Brunet, and M. K. Yau (2003), Spiral bands in a simulated hurricane: part II wave activity diagnostics, *Journal of Atmospheric Sciences*, *60*, 1239–1256.

Dritschel, D. G. (1988), Contour surgery: a topological reconnection scheme for extended integrations using contour dynamics, *Journal of Computational Physics*, *77*, 240–266.

Dritschel, D. G. (1989), Contour dynamics and contour surgery: numerical algorithms for extended, high-resolution modelling of vortex dynamics in two-dimensional, inviscid, incompressible flows, *Computer Physics Reports*, *10*, 77–146.

Dritschel, D. G. (1995), A general theory for two-dimensional vortex interaction, *Journal of Fluid Mechanics*, *293*, 269–303.

Dritschel, D. G., and M. H. P. Ambaum (1997), A contour-advective semi-Lagrangian numerical algorithm for simulating fine-scale conservative dynamical fields, *Quarterly Journal of the Royal Meteorological Society*, *123*, 1097–1130.

Dritschel, D. G., and D. W. Waugh (1992), Quantification of the inelastic interaction of unequal vortices in two-dimensional vortex dynamics, *Physics of Fluids*, *A 4*, 1737–1744.

Ferreira, R. N., and W. H. Schubert (1999), The role of tropical cyclones in the formation of tropical upper-tropospheric troughs, *Journal of Atmospheric Sciences*, *56*, 2891–2907.

Grazzini, F., and G. van der Grijn (2002), Central European floods during summer 2002, *Tech. rep.*, European Centre for Medium-Range Weather Forecast, ECMWF newsletter.

Guinn, T., and W. Schubert (1993), Hurricane spiral bands, *Journal of Atmospheric Sciences*, *50*, 3380–3404.

Habjan, E. E., and G. J. Holland (1995), Extratropical transition of tropical cyclones in the western Australia region, in *21'st Conference on Hurricanes and Tropical Meteorology*, American Meteorology Society, Miami, Florida.

Haynes, P. H. (1989), The effect of barotropic instability on the non-linear evolution of a Rossby wave critical layer, *Journal of Fluid Mechanics*, *207*, 231–266.

Holton, J. R. (1992), *An Introduction to Dynamic Meteorology*, forth ed., Academic Press.

Hoskins, B. J., and T. Ambrizzi (1993), Rossby-wave propagation on a realistic longitudinally varying flow, *Journal of Atmospheric Sciences*, *50*, 1661–1671.

Hoskins, B. J., and P. Berrisford (1988), A potential vorticity view of the storm of 15-16 October 1987, *Weather*, *43*, 122–129.

Hoskins, B. J., M. E. McIntyre, and A. W. Robertson (1985), On the use and significance of isentropic potential vorticity maps, *Quarterly Journal of the Royal Meteorological Society*, *111*, 877–946.

Jones, S. C., et al. (2003), The extratropical transition of tropical cyclones: forecast challenges, current understanding, and future directions, *Weather and Forecasting*, *18*, 1052–1092.

Keyser, D., B. D. Schmidt, and D. G. Duffy (1992), Quasigeostrophic diagnosis of three-dimensional ageostrophic circulation in an idealized baroclinic disturbance, *Monthly Weather Review*, *120*, 698–730.

Krishnamurti, Y., T. S. V. Vijaya Kumar, K. Rajendran, and A. Hopkins (2003), Antecedents of the flooding over south-eastern England during October 2000, *Weather*, *58*, 367–370.

Lawrence, M. B. (1996), Preliminary report - hurricane Luis 27 August - 11 September 1995, www.nhc.noaa.gov/1995luis.html - NOAA National Hurricane Center tropical cyclones preliminary reports.

Lawrence, M. B. (2000), Preliminary report - hurricane Gert 11-23 September 1999, www.nhc.noaa.gov/1999gert.html - NOAA National Hurricane Center tropical cyclones preliminary reports.

Macaskill, C., W. E. P. Padden, and D. G. Dritschel (2003), The CASL algorithm for quasi-geostrophic flow in a cylinder, *Journal of Computational Physics*, *188*, 232–251.

MacDonald, N. J. (1968), The evidence of the existence of Rossby like waves in the hurricane vortex, *Tellus*, *20*, 138–150.

Martius, O. C. (2005), Climatological aspects of wave disturbances on the tropopause and links to extreme weather in Europe, Ph.D. thesis, Swiss Federal Institute of Technology (ETH) - Zurich.

McWilliams, J. C., P. R. Gent, and N. J. Norton (1986), The evolution of balanced, low-mode vortices on the beta-plane, *Journal of Atmospheric Sciences*, *16*, 838–855.

Montgomery, M. T., and R. J. Kallenbach (1997), A theory for vortex-Rossby waves and its application to spiral bands and intensity changes in hurricanes, *Quarterly Journal of the Royal Meteorological Society*, *123*, 435–465.

Nakamura, M., and R. A. Plumb (1994), The effects of flow asymmetry on the direction of Rossby wave breaking, *Journal of Atmospheric Sciences*, *51*(14), 2031–2045.

Norton, W. A. (1994), Breaking Rossby waves in a model stratosphere diagnosed by a vortex-following coordinate system and a technique for advecting material contours, *Journal of Atmospheric Sciences*, *51*, 654–673.

Pasch, R. J. (1999), Preliminary report - hurricane Jose 17-25 October 1999, www.nhc.noaa.gov/1999jose.html - NOAA National Hurricane Center tropical cyclones preliminary reports.

Pedlosky, J. (1987), *Geophysical Fluid Dynamics*, second ed., Springer.

Petterssen, S., and S. J. Smebye (1971), On the development of extratropical cyclones, *Quarterly Journal of the Royal Meteorological Society*, *97*, 457–482.

Polvani, L. M., and R. A. Plumb (1992), Rossby wave breaking, microbreaking, filamentation, and secondary vortex formation: the dynamics of a perturbed vortex, *Journal of Atmospheric Sciences*, *49*, 462–476.

Pratt, L. J., and M. E. Stern (1986), Dynamics of potential vorticity fronts and eddy detachment, *Journal of Physical Oceanography*, *16*, 1099–1118.

Schwierz, C., S. Dirren, and H. C. Davies (2004), Forced waves on a zonally aligned jet stream, *Journal of Atmospheric Sciences*, *61*(1), 73–87.

Scott, R. K., D. G. Dritschel, L. M. Polvani, and D. W. Waugh (2004), Enhancement of Rossby wave breaking, by steep potential vorticity gradients in the winter stratosphere, *Journal of Atmospheric Sciences*, *61*, 904–918.

Shapiro, M. A. (2004), A societal/economic impact perspective of Rossby wave-train propagation for the extreme northern-hemisphere weather events of November 2002, *Tech. rep.*, American Meteorology Society, 84th AMS Annual Meeting, Seattle, WA.

Shapiro, M. A., and A. J. Thorpe (2004), THORPEX international science plan, *Tech. rep.*, World Meteorological Organization, WWRP/THORPEX No. 2.

Stern, M. E., and L. J. Pratt (1985), Dynamics of vorticity fronts, *Journal of Fluid Mechanics*, *161*, 513–532.

Swanson, K. L., P. J. Kushner, and I. M. Held (1997), Dynamics of barotropic storm tracks, *Journal of Atmospheric Sciences*, *54*, 791–810.

Thorncroft, C. D., B. J. Hoskins, and M. E. McIntyre (1993), Two paradigms of baroclinic wave life cycle behaviour, *Quarterly Journal of the Royal Meteorological Society*, *119*, 17–55.

Vosbeek, P. W. C. (1998), Contour dynamics and applications to 2d vortices, Ph.D. thesis, Eindhoven University of Technology - Eindhoven.

Waugh, D. W., and R. A. Plumb (1994), Contour advection with surgery: a technique for investigating finescale structure in tracer transport, *Journal of Atmospheric Sciences*, *51*, 530–540.

Zabusky, N. J., M. H. Hughes, and K. V. Roberts (1979), Contour dynamics for the Euler equations in two dimensions, *Journal of Computational Physics*, *135*, 220–226.